Noname manuscript No.
(will be inserted by the editor)

Prediction and validation of aeroelastic limit cycle oscillations using harmonic balance methods and Koopman operator

Michael McGurk · Jie Yuan

Received: date / Accepted: date

Abstract Nonlinearities in aerospace systems often induce self-sustaining oscillations known as Limit Cycle Oscillations (LCO), requiring costly analyses for identification. A major challenge is the computational expense of generating bifurcation diagrams, which limits the feasibility of nonlinear analysis in early design phases. This restriction not only constrains design possibilities but also impedes data-driven methods for nonlinear aeroelastic analysis, which rely on efficient data collection—a growing focus in the aerospace sector. This work proposes a computationally efficient numerical framework to predict LCO amplitudes and assess stability in nonlinear aeroelastic systems. The approach integrates the Harmonic Balance Method (HBM) with the Hill method for stability analysis. To address the sorting problem, a Koopman operator-based data-driven method is employed. The framework is validated using numerical test cases with both smooth and nonsmooth nonlinearities, benchmarked against results from MATCONT, COCO and time-domain simulations. Finally, experimental validation is performed by comparing the framework's predictions with LCO experimental data obtained through control-based continuation experiments.

Keywords Nonlinear Aeroelasticity · Numerical continutation · Stability analysis

M. McGurk
Aerospace Centre of Excellence
Department of Mechanical and Aerospace Engineering
University of Strathclyde, Glasgow, G1 1XQ, UK
E-mail: michael.mcgurk@strath.ac.uk

J. Yuan
Corresponding author
Computational Engineering Design Group
Department of Aeronautics and Astronautics Engineering
University of Southampton,Southampton, SO17 1BJ, UK
E-mail: j.yuan@soton.ac.uk

1 Introduction

With the increasing integration of lightweight materials and complex systems, the study of nonlinearities in aerospace structures has become an important area of research. These nonlinearities are typically classified into two categories: geometric nonlinearities, which manifest throughout the entire structure, and localised nonlinearities, which are confined to specific areas [49, 45, 35]. Geometric nonlinearities often arise from large deflections induced by the use of lightweight materials [46], while localised nonlinearities can stem from factors such as friction within structural joints, becoming more prevalent as complex novel systems are integrated [26, 20]. The effects of these nonlinearities on dynamics and control can be significant, altering flutter boundaries in tiltrotor systems and shifting the aerodynamic centre of certain wings, thereby affecting control strategies [38, 50].

A common phenomenon resulting from both forms of nonlinearities is the occurrence of self-sustaining oscillations known as Limit Cycle Oscillations (LCO). Both theoretical analysis and experimental evidence indicate that close to the linear flutter velocity of aeroelastic systems the formation of LCO occur [22, 57]. These LCO often represent the maximum response of systems, with significant implications for structural fatigue, making them crucial to track [18]. Moreover, the stability of LCO is essential to consider, as stable LCO signify real physical oscillations towards which the system can converge, while unstable LCO indicates orbits where the perturbed response diverges [60].

However, determining LCO behaviour typically involves costly nonlinear analysis, particularly through the generation of bifurcation diagrams. Both generating these diagrams and determining stability can be resource-intensive, leading to the neglect of nonlinear analysis in early design stages and constraining the potential design space [37]. Furthermore, this limitation hampers nonlinear aeroelastic analysis through data-driven approaches, which rely on efficient gathering of training data and have garnered attention in the aerospace industry [40, 51, 56]. Therefore, there is a demand for computationally efficient methods to determine LCO behaviour in aeroelastic systems.

This study aims to propose a computationally efficient method for estimating LCO behaviour and determining their stability in aeroelastic systems. This is accomplished by conducting LCO analysis solely in the frequency domain, combining HBM continuation with Koopman operator based stability analysis. To validate the proposed method numerically, the comparison is made with state-of-the-art time-domain solvers, namely MATCONT [14] and COCO [3], in both smooth and nonsmooth nonlinear case studies. Additionally, the framework is experimentally validated by comparing predicted LCO behaviour with empirical LCO data.

The onset of LCO typically arises at a specific type of bifurcation known as a Hopf bifurcation [54]. Both theoretical analyses and experimental investigations have demonstrated that Hopf bifurcations coincide with the flutter points of aeroelastic systems [22, 57]. The numerical continuation process leverages previous solutions of the system and the equations of motion to accurately

predict subsequent solutions with respect to a chosen continuation parameter. Various methods, primarily employing a predictor-corrector approach, have been developed to provide rough estimates followed by refinement for improved accuracy. Among these, methods such as arclength and pseudoarclength continuation have proved effective in tracing solutions beyond turning points, thereby revealing diverse system behaviours. Despite differences in existing bifurcation software, the predominant tools rely on orthogonal collocation methods for tracking and modelling LCO [8]. Orthogonal collocation, a time-domain method, segments a periodic orbit into intervals, represents unknown variables using polynomials on each interval, and collocates the governing equations at Gauss points [27]. Orthogonal collocation techniques are integrated into widely used bifurcation software packages such as MATCONT, AUTO, and COCO [15,17,12]. However, despite their accuracy, these methods are seldom applied to larger systems due to substantial memory requirements, leading to high computational costs.

Harmonic balance methods (HBM) offer a computationally efficient alternative for identifying the maximum response of LCO. In HBM, the periodic motion of LCO is approximated using Fourier series coefficients in the frequency domain. The Alternative Frequency Time scheme (AFT) is implemented so different types of nonlinear forces can be evaluated in the frequency domain [9]. Unlike time-domain methods, where a set of coordinates with corresponding time values must be stored to characterise the response, HBM requires storing only a set number of coefficients. The method is tailored for analysing periodic responses in systems with strong nonlinearities, particularly when time-domain simulations become computationally expensive. Key challenges in its application include ensuring convergence, managing computational costs for higher harmonic orders, and accurately modelling non-smooth nonlinearities. Previous studies [23,52] have demonstrated that HBM can achieve a high level of accuracy compared to alternative methods like the shooting method while being significantly less computationally expensive. In a comparison between HBM and orthogonal collocation on nonlinear mechanical systems, Karkar found HBM to exhibit better convergence on certain systems and to be "very robust" [27]. However, the literature lacks comprehensive research comparing HBM to current alternatives, particularly in the context of aeroelasticity [13,27]. Existing studies are mostly confined to low-harmonics or focus on forced non-autonomous systems [30]. Although the NLvib package implements HBM, its primary focus is on nonlinear mechanical systems, and it does not include stability analysis purely in the frequency domain [28].

The conventional estimation of LCO stability typically involves time domain methods, such as Floquet analysis, as highlighted in Ref [53]. However, as frequency domain methods gain prominence in LCO analysis, there is a growing interest in techniques that directly compute stability in the frequency domain. Guillot et al. [24,32] demonstrated the use of the Hill's matrix for computing the stability of LCO modeled by Fourier series through eigenvalue analysis. Lazarus and Thomas demonstrated the method's accuracy on a forced Duffing oscillator system [31]. While effective, this method tends to be compu-

tationally demanding, especially when dealing with large numbers of harmonic orders necessary for modelling complex nonlinear systems, leading to extended computation times. For large-scale scenarios, stability analysis using the Hill method can be more numerically costly than computing periodic motion [29, 48]. The applications of Koopman operator methods to limit cycling systems have been explored for stability analysis [39,42]. Additionally, they have been applied to jet engine instabilities with the advent of data-driven methods [43]. In recent developments, the Koopman operator has been employed to derive the monodromy matrix directly from Hill's matrix, as elucidated by Bayer and Leine [6]. In the Koopman framework, the dynamical system is characterised by the evolution of functions on the state space over time. This method elevates the problem to a higher-dimensional space where the system demonstrates more predictable behaviour. This innovative approach significantly reduces the number of eigenvalues needed for stability computation, aligning it with the number of degrees of freedom in the system. Consequently, this advancement holds promise for enhancing the efficiency of stability analysis in the frequency domain. However, it has not been applied and validated to nonlinear smooth dynamical systems.

This paper presents the methodology for a general aeroelastic frequency domain solver for LCO. The methodology encompasses a detailed explanation of the HBM continuation scheme and frequency domain stability analysis. The preliminary numerical findings of this research were showcased at the conference [41]. This paper comprehensively outlines the HBM methodology, incorporating Koopman operator based stability analysis for predicting LCO behaviours. Subsequently, the methodology is applied to a numerical test case, incorporating both smooth and nonsmooth nonlinearities. The test case results are then validated by comparison with outcomes from MATCONT and COCO software. Following numerical validation, the framework's results are juxtaposed with LCO experimental data obtained through Control Based Continuation (CBC) experiments [7]. Ultimately, conclusions are drawn based on the numerical and experimental validation of the proposed framework.

2 Methodology

In this section, the computational framework based on HBM and Koopman operator based stability analysis is presented. First, the standard mathematical format is introduced, laying out the basic principles behind HBM continuation based on the work in Ref [16]. The AFT procedure is then outlined, as it is essential to all steps of this methodology. Finally, two methods of determining LCO stability in the frequency domain are described: the standard Hill's method and Koopman operator based analysis.

2.1 General equation of motion

The methods outlined here revolve around mathematical models that can be formulated into the second-order differential equation depicted in Equation 1. Nonlinear aeroelastic systems can be organised in this manner under the assumption that structural forces counterbalance aerodynamic forces.

$$M\ddot{x} + D\dot{x} + Kx + q_{nl}f_{nl} = A\ddot{x} + B\dot{x} + Cx \tag{1}$$

Degrees of freedom of the system are denoted as x, while M, D, and K represent the structural mass, damping, and stiffness matrices, respectively. Matrices A, B, and C characterise the encountered aerodynamic force, with a size of $N \times N$, where N is the number of degrees of freedom of the system. The nonlinear function f_{nl} captures various types of nonlinearities encountered in aeroelastic systems. The $N \times 1$ vector q_{nl} incorporates the nonlinear equations affecting the degrees of freedom. The standard differential equation is restructured into a first-order state equation, as shown in Equation 2:

$$\dot{\mathbf{x}} = \mathbf{Q}\mathbf{x} + \mathbf{q}_n f_{nl} \tag{2}$$

Where:

$$\mathbf{x} = \begin{bmatrix} \dot{x} \\ x \end{bmatrix} \mathbf{Q} = \begin{bmatrix} (M-A)^{-1}(B-D) & (M-A)^{-1}(C-K) \\ 0_{N\times N} & I_{N\times N} \end{bmatrix} \mathbf{q_n} = \begin{bmatrix} -(M-A)^{-1}q_{nl} \\ 0_{N\times 1} \end{bmatrix} \tag{3}$$

The matrix $\mathbf{Q}$ will be denoted as the linear matrix, as it completely represents the linear dynamics of the system. This structural arrangement facilitates the conduct of linear analysis to identify the flutter point through the following procedure. By focusing solely on the linear aspect of the system, Equation 2 can be expressed as the eigenvalue problem $\dot{\mathbf{x}} - \mathbf{Q}\mathbf{x} = 0$. Assuming an oscillatory response $x = x_o e^{\psi t}$, the eigenvalue problem is formulated as:

$$[\mathbf{Q} - \mathbf{I}\psi_{ij}]\,\phi = 0 \tag{4}$$

Where ψ_{ij} are eigenvalues in the conjugate pair

$$\psi_{ij} = -\zeta_{ij}\omega_{ij} \pm i\omega_{ij}\sqrt{1-\zeta_{ij}} \tag{5}$$

The undamped natural frequencies are denoted by ω_{ij}, while ζ_{ij} represents the damping ratios. Matrix ϕ encompasses the corresponding eigenvectors. Flutter manifests as unstable, negatively damped oscillations. Based on this characterisation, it becomes evident that if any of the real parts of Equation 5 are positive, the system exhibits dynamic instability [61].

2.2 Harmonic Balance Method

Incorporating nonlinearities alters this behavior. In nonlinear systems, the loss of linear stability typically leads to the emergence of LCO at a hopf bifurcation point. While linear analysis can pinpoint hopf bifurcation points, numerical continuation from such points often reveals the presence of LCO solutions even before the loss of linear stability.

Assuming that the system's dynamic response after a hopf bifurcation is an LCO, we can represent the time response of x and $\dot{x}$ using the Fourier series. The system can then be expressed through multi-harmonic response and solved in the frequency domain:

$$x(t) = X_0 + \sum_{k=1}^{l} X_{k,s} \sin k\omega t + X_{k,c} \cos k\omega t \tag{6}$$

The variable l denotes the harmonic order of the response, while X_0, $X_{k,s}$, and $X_{k,c}$ represent Fourier coefficients. This assumed response is fundamental to HBM, facilitating the transformation of the system from the time domain to the frequency domain. Instead of necessitating a time integration process spanning potentially hundreds to thousands of time steps, only $N \times (2l + 1)$ steps are required to characterise the dynamic behaviour of the system.

An additional step is necessary to model the nonlinear force component of Equation 2. Nonlinear forces are typically depicted as nonlinear time functions. Since they do not adhere to linearity with respect to states or represent explicit functions of time, direct transformation to the frequency domain is impractical [9]. However, the nonlinear force response can be transformed to the frequency domain via the AFT procedure, facilitating the determination of F_0, $F_{k,s}$, and $F_{k,c}$ as:

$$f_{nl}(t) = F_0 + \sum_{k=1}^{l} F_{k,s} \sin k\omega t + F_{k,c} \cos k\omega t \tag{7}$$

The predicted values of X_0, $X_{k,s}$, $X_{k,c}$, and ω are utilised in Equation 6 to derive the time domain response over a period. Subsequently, the time domain nonlinear force response $f_{nl}(t)$ is determined. A fast Fourier transform algorithm (FFT) is then applied to estimate Fourier coefficients based on the time domain nonlinear force response. This is commonly known as the AFT procedure, laid out in Figure 1. Leveraging these relationships, the equation of motion depicted in Equation 2 can be reformulated into a set of algebraic residual equations, which are solved numerically. Accuracy can be assessed through convergence studies and benchmarking against numerical tools such as COCO and MATCONT. A converged HBM result with respect to l can generally be assumed to be reliable for the system under consideration, in the absence of such comparisons.

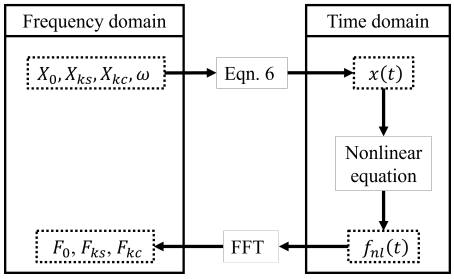

Fig. 1: AFT procedure

2.3 Continuation scheme

A continuation scheme is formulated based on the principles of HBM. Its aim is to determine the amplitude and frequency of LCO, along with their corresponding values of a chosen continuation parameter. Given the uncertainty in the shape of the bifurcation diagram, both the continuation parameter λ and LCO frequency ω are treated as unknowns in this scheme. Typically, in an aeroelastic system, velocity is used as the continuation parameter. It is worth noting that the linear system matrix $\mathbf{Q}$ is often dependent on the continuation parameter. The equations of motion in the nonlinear degrees of freedom are denoted as follows:

$$\ddot{x}_{nl}(t) = (\mathbf{Q})_{u,p}\mathbf{x}_L + (\mathbf{Q})_{u,u}\dot{x}_{nl}(t) + (\mathbf{Q})_{u,v}x_{nl}(t) + (\mathbf{q}_n)_u f_{nl}(t) \tag{8}$$

Linear Fourier coefficients, denoted by $\mathbf{x}_L = [\overline{X}0, \overline{X}_{k,s}, \overline{X}_{k,c}]$, are obtained by solving only the linear components of the system. Here, the linear degrees of freedom or modes are labeled as p, while the nonlinear degrees of freedom and modes are designated as u and v, respectively. Substituting Equation 6 into Equation 8 yields the set of $N \times (2l+1)$ residual equations:

$$\begin{aligned}
R_0 &= (\mathbf{Q})_{u,p}\overline{X}_0 + (\mathbf{Q})_{u,v}X_0 + (\mathbf{q}_n)_u F_0 \\
R_{k,s} &= -k^2\omega^2 X_{k,s} - (\mathbf{Q})_{u,p}\overline{X}_{k,s} - (\mathbf{Q})_{u,u}k\omega X_{k,c} - (\mathbf{Q})_{u,v}X_{k,s} - (\mathbf{q}_n)_u F_{k,s} \\
R_{k,c} &= -k^2\omega^2 X_{k,c} - (\mathbf{Q})_{u,p}\overline{X}_{k,c} + (\mathbf{Q})_{u,u}k\omega X_{k,s} - (\mathbf{Q})_{u,v}X_{k,c} - (\mathbf{q}_n)_u F_{k,c}
\end{aligned} \tag{9}$$

In scenarios involving multiple nonlinear degrees of freedom, a set of $N \times (2l+1)$ residual equations are derived for each nonlinear degree of freedom. Incorporating λ and ω as unknowns necessitates formulating two additional residual equations. A common constraint imposed on the scheme is related to pseudo-arclength continuation [4,11]. Using point j as the reference in the continuation, a prediction for $j+1$ is generated utilising tangential direction vectors. It is assumed that the converged solution for $j+1$ is orthogonal to the initial prediction, imposing the following constraint in the corrector stage

during the numerical continuation:

$$R_{2l+2} = (X_{j+1} - X_{j+1,0})\frac{dX}{ds}_j + (\omega_{j+1} - \omega_{j+1,0})\frac{d\omega}{ds}_j + (\lambda_{j+1} - \lambda_{j+1,0})\frac{d\lambda}{ds}_j \quad (10)$$

Through this constraint, direction vectors ($\frac{d(X,\omega,\lambda)}{ds}$ where s denotes the non-dimensional arc-length) for the next continuation step are also obtained.

Another widely used constraint is based on the principle of orthogonality between the phase of degrees of freedom and their rates of change [27,21]. This assumption can be used to derive a relationship between j^{th} Fourier coefficients and the $j+1$ points:

$$R_{2l+3} = \sum_{k=1}^{l} -k(X_{k,c})_j(X_{k,s})_{j+1} + k(X_{k,s})_j(X_{k,c})_{j+1} \quad (11)$$

Both of these constraints are commonplace in continuation methods and are also employed in time-domain methods. Further details on each can be found in Ref [16,12]. With an equal number of residual equations and unknowns $[X_0, X_{k,s}, X_{k,c}, \omega, \lambda]$ (for $k = 1, \ldots, l$), the system can be numerically solved at each point in the continuation.

The system can be solved iteratively typically through the Newton–Raphson procedure [16]. This involves linking displacements to rates of change through the Jacobian matrix $J = d\dot{\mathbf{x}}/d\mathbf{x}$ via $\dot{\mathbf{x}} = J\mathbf{x}$. While the Jacobian can be numerically evaluated through finite difference methods, this approach can be computationally demanding, particularly for large-scale systems [55]. Alternatively, the analytical Jacobian can be incorporated by defining it via a Fourier transform [13].

$$J(t) = J_0 + \sum_{k=1}^{l} J_{k,s} \sin k\omega t + J_{k,c} \cos k\omega t \quad (12)$$

From Equations 1 and 6 we can derive the Jacobi for each Harmonic order as:

$$\begin{aligned} \mathbf{J}_0 &= \mathbf{Q} + \mathbf{q}_n \left(\frac{\partial F}{\partial X}\right)_0 \\ \mathbf{J}_{k,s} &= \mathbf{Q} + \mathbf{q}_n \left(\frac{\partial F}{\partial X}\right)_{k,s} \\ \mathbf{J}_{k,c} &= \mathbf{Q} + \mathbf{q}_n \left(\frac{\partial F}{\partial X}\right)_{k,c} \end{aligned} \quad (13)$$

Approximations for $\left(\frac{\partial F}{\partial X}\right)_0$, $\left(\frac{\partial F}{\partial X}\right)_{k,s}$, and $\left(\frac{\partial F}{\partial X}\right)_{k,c}$ can be achieved by analytically transforming the time-domain derivation $\frac{df_{nl}}{d\mathbf{x}}(t)$ into the frequency domain using the inverse Fast Fourier Transform procedure.

$$\frac{df_{nl}}{d\mathbf{x}}(t) = \left(\frac{\partial F}{\partial X}\right)_0 + \sum_{k=1}^{l} \left(\frac{\partial F}{\partial X}\right)_{k,s} \sin k\omega t + \left(\frac{\partial F}{\partial X}\right)_{k,c} \cos k\omega t \quad (14)$$

This necessity arises solely within the nonlinear degrees of freedom. An added advantage is that the Fourier coefficients of the Jacobian can be utilised to directly assess the stability of the response in the frequency domain, as elaborated in the subsequent section.

2.4 Frequency domain stability determination

Once a converged solution including LCO amplitude, frequency, and continuation parameter is achieved in the frequency domain, the stability of the oscillation must be determined. A stable LCO solution describes behavior where, following an initial perturbation, the system's response is drawn towards the LCO. Conversely, with an unstable LCO, the response moves away from the unstable cycle [47].

Time-domain analysis is used as a reference in the study, which relies on the use of monodromy matrix Φ_T $(N \times N)$ to assess the stability of the system through its evolution in state changes over time. The monodromy matrix is illustrated in Equation 15 which portrays the evolution of the system's states over a single period T. It can usually be obtained as a byproduct of time-domain continuation processes where the stability of the system can be subsequently assessed based on its eigenvalues known as Floquet multipliers [58]. If the absolute value of any of the N Floquet multipliers exceeds 1, the system is deemed unstable. This approach is herein referred to as time-integration stability analysis.

$$\mathbf{x}_T = \Phi_T \mathbf{x}_0 \tag{15}$$

2.4.1 Hill's method

In the frequency domain, the stability of an oscillation can be computed using Hill's method, which still applies Floquet theory [47]. The stability is determined based on the eigensolution of the truncated Hill's matrix $\mathbf{H}$ as follows:

$$\mathbf{H}_\infty = \begin{pmatrix} \ddots & \vdots & \vdots & \vdots & \iddots \\ \dots & \mathbf{J}_0 + \omega\mathbf{I} & \mathbf{J}_{1,s} & \mathbf{J}_{2,s} & \dots \\ \dots & \mathbf{J}_{1,c} & \mathbf{J}_0 & \mathbf{J}_{1,s} & \dots \\ \dots & \mathbf{J}_{2,c} & \mathbf{J}_{1,c} & \mathbf{J}_0 - \omega\mathbf{I} & \dots \\ \iddots & \vdots & \vdots & \vdots & \ddots \end{pmatrix} \tag{16}$$

The Hill's matrix is truncated to size $N(2l+1) \times N(2l+1)$:

$$\mathbf{H} = \begin{pmatrix} \mathbf{J}_0 + l\omega\mathbf{I} & \dots & \mathbf{J}_{-2l} \\ \vdots & \ddots & \vdots \\ \mathbf{J}_{2l} & \dots & \mathbf{J}_0 - l\omega\mathbf{I} \end{pmatrix} \tag{17}$$

Assuming $J_{k,s}$ and $J_{k,c}$ for $k > l$ are $N \times N$ zero matrices, as per standard Hill's method. N terms, referred to as Floquet exponents (distinct from Floquet multipliers), are subsequently selected from the $N(2l+1)$ eigenvalues

of the matrix $\mathbf{H}$ [32]. A numerical sorting algorithm is employed to identify eigenvalues corresponding to $k = 0$. The conventional approach involves sorting the eigenvalues based on the amplitude of their imaginary parts. The N eigenvalues with the smallest amplitude of imaginary parts are then selected as the Floquet exponents. Stability is determined by comparing the real parts of the Floquet exponents to zero. For the system to be deemed dynamically stable, all real parts must be below zero; otherwise, the system is unstable.

2.4.2 Koopman operator based stability analysis

Koopman lift theory can be introduced to reduce the computational cost of frequency domain stability analysis. The Koopman operator stability process operates under two assumptions to derive an approximation of the monodromy matrix. The first assumption is that the higher-dimensional space z can be utilised to estimate the lower-dimensional space $\mathbf{x}$ via:

$$\mathbf{x}(t) \approx \mathbf{x}_z(t) = \mathbf{C}(t)z(t) \tag{18}$$

Here, $\mathbf{C}(t)$ represents the time-dependent projection matrix that fulfils the condition $\mathbf{C}(t)z(t) = \mathbf{x}_z(t)$, with $z(t)$ composed of monomial terms and Fourier terms of the base frequency [6]. $z(t)$ can be then expressed as:

$$z(t) = \begin{pmatrix} Z_{-l}^1 e^{-il\omega t} \\ \vdots \\ Z_l^1 e^{il\omega t} \\ Z_{-l}^2 e^{-il\omega t} \\ \vdots \\ Z_l^N e^{il\omega t} \end{pmatrix} \tag{19}$$

Where l is the maximum frequency order, N is the maximum index of the monomial term and Z_l^N is the l^{th} Fourier coefficient of the N^{th} monomial term. The dimension of this orthogonal basis functions $z(t)$ is $N(2l+1)$. Here, these linear basis functions are ordered by the state at first and then by the frequency in an ascending order. Vector $\mathbf{Z}_l$ is used to denote the vector containing the Fourier coefficients corresponding to the l^{th} frequency for each monomial term.

A common choice for the projection matrix $\mathbf{C}(t)$ in frequency-based projection is to select the zeroth harmonic, which corresponds to the steady-state or average behavior of the system providing insight into the system's mean behaviour or equilibrium states [6]. To select the components related to the zeroth harmonic of $z(t)$, the frequency domain projection matrix is defined as:

$$\tilde{\mathbf{C}} = (\mathbf{0} \dots \mathbf{0}\ \mathbf{I}_{n\times n}\ \mathbf{0} \dots \mathbf{0}) \tag{20}$$

The second assumption of the Koopman operator-based stability method is that the truncated Hill's matrix can be utilised to derive the state transition matrix of the high-dimensional space with [6]:

$$z(t) = \mathbf{U}^{\mathrm{T}} e^{\mathbf{H}t} \mathbf{U} z(0) \tag{21}$$

Where $\mathbf{U}$ is the transformation matrix to convert the Hill's matrix from frequency to time domain, satisfying the criteria $\mathbf{U}z(t) = (\mathbf{Z}_{-l}e^{il\omega t} \dots \mathbf{Z}_l e^{-il\omega t})^{\mathrm{T}}$. Substituting Equations 18 into 21 yields the following expression:

$$\mathbf{x}_z(t) = \mathbf{C}(t)\mathbf{U}^{\mathrm{T}} e^{\mathbf{H}t}\mathbf{U}z(0) \tag{22}$$

At $t = 0$, Equation 19 simplifies to $z(0) = \tilde{\mathbf{W}}\mathbf{x}(0)$, where:

$$\tilde{\mathbf{W}} = \begin{pmatrix} \mathbf{I}_{n\times n} \\ \vdots \\ \mathbf{I}_{n\times n} \end{pmatrix} \tag{23}$$

Utilising both reductions matrices together in Equation 22, results in:

$$\mathbf{x}_z = C(t)\mathbf{U}^{\mathrm{T}} e^{\mathbf{H}t}\mathbf{U}\mathbf{W}\mathbf{x}(0) \tag{24}$$

Over a full period T this yields:

$$\mathbf{x}_T \approx \tilde{\mathbf{C}} e^{\mathbf{H}t}\tilde{\mathbf{W}}\mathbf{x}_0 \tag{25}$$

As per Equation 15, this implies that the monodromy matrix can be approximated in the frequency domain by:

$$\Phi_T \approx \tilde{\mathbf{C}} e^{\mathbf{H}T}\tilde{\mathbf{W}} \tag{26}$$

This approximation of the monodromy matrix enables the computation of system stability through Floquet multipliers, employing the same method as in standard time-domain stability analysis. Thus, compared to traditional Hill's stability analysis, utilising the Koopman operator reduces the necessary number of eigenvalues from $N(2H + 1)$ to just N. This approach will be referred to herein as Koopman operator-based stability analysis.

Figure 2 provides an overview of the complete HBM continuation process, including stability analysis. The continuation starts with an initial estimate of the LCO frequency from eigenvalue analysis and a small guess for the amplitude. Nonlinear forces are then computed in the frequency domain using the AFT procedure, which estimates the system's linear degrees of freedom. The residual equations 9, 10 and 11 are numerically solved. Once a converged solution is achieved, stability analysis is performed using either Hill's method or the Koopman-based procedure. Direction vectors are calculated through finite differences based on previous points in the continuation scheme, and these vectors are used to estimate the next point via the tangent predictor method [16]. This process continues until a user-defined stopping criterion is met, such as the number of points or maximum/minimum continuation parameter.

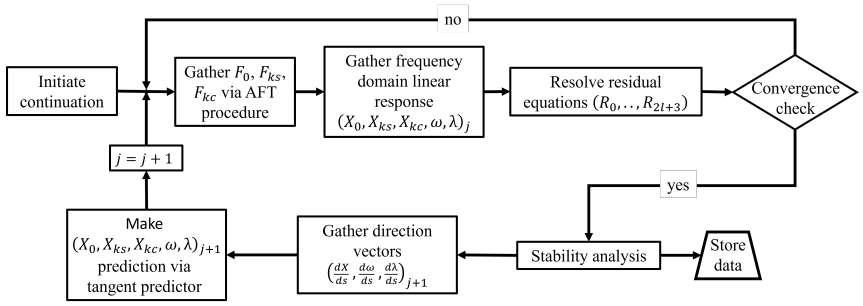

Fig. 2: HBM continuation process with stability analysis

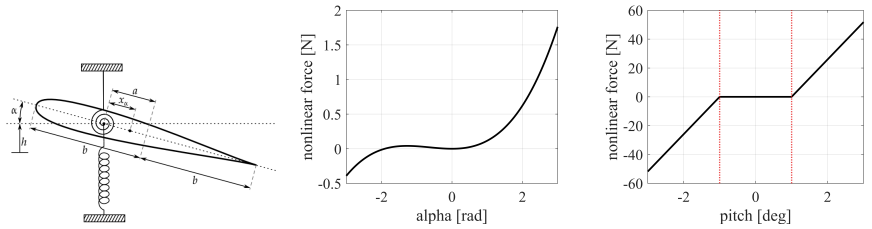

(a) (b) (c)

Fig. 3: Numerical test case (a) Freebody diagram of 2 DoF aerofoil [34], (b) Quadractic-Cubic nonlinearity, (c) Freeplay nonlinearity with $\delta = 1^o$

3 Test case

The model under investigation here is a simplified representation of the system analysed in Ref. [36], focusing on a two-degree-of-freedom aerofoil section depicted in Figure 3a. In this model, the degrees of freedom are the pitch angle α and the heave h. The plunge degree-of-freedom is governed by a spring with stiffness K_h, while a torsional spring K_α resists pitch movement. For the nonlinear flutter rig considered, the state variables are denoted as $x = [h, \alpha, w]$, where h represents heave, α denotes pitch, and w indicates the aerodynamic state. The structural matrices, as shown in Equation 1, are configured as follows:

$$\mathbf{M} = \begin{bmatrix} m_T & m_w x_\alpha b & 0 \\ m_w x_\alpha b & I_\alpha & 0 \\ 0 & 0 & 1 \end{bmatrix}; \quad \mathbf{D} = \begin{bmatrix} c_h & 0 & 0 \\ 0 & c_\alpha & 0 \\ -1/b & a - 1/2 & 0 \end{bmatrix}; \quad \mathbf{K} = \begin{bmatrix} K_h & 0 & 0 \\ 0 & K_\alpha & 0 \\ 0 & 0 & 0 \end{bmatrix} \tag{27}$$

Aerodynamic matrices are derived from the unsteady aerodynamic model described by Abdelkef et al. [2].

$$\mathbf{A} = \begin{bmatrix} -\pi b^2 & a\pi b^3 & 0 \\ a\pi b^3 & -\pi\left(1/8 + a^2\right) b^4 & \\ 0 & 0 & 1 \end{bmatrix}$$
$$\mathbf{B} = \begin{bmatrix} -\pi bC(k) & -\left(1 + (1/2 - a)\right)\pi b^2 C(k)/\rho & -2\pi Vb\left(c_1c_2 + c_3c_4\right)/\rho \\ \pi\left(a + 1/2\right) b^2/V & -\left(1/4 - a^2\right)\pi b^3 & 2\pi b^2 V\left(a + 1/2\right)\left(c_1c_2 + c_3c_4\right) \\ 0 & 0 & -\left(c_2 + c_4\right)/\rho b \end{bmatrix}$$
$$\mathbf{C} = \begin{bmatrix} 0 & -\pi bC(k) & -2\pi Vc_2c_4\left(c_1 + c_3\right)/\rho \\ 0 & \pi b^2 C(k)\left(1/2 + a\right) & 2\pi b\left(a + 1/2\right)c_2c_4\left(c_1 + c_3\right) \\ 0 & 1/\rho Vb & c_2c_4/\rho b^2 \end{bmatrix} \tag{28}$$

Where $C(k)$ is the generalised Theodorsen's function detailed in Ref.[59]. Theodrsen's function is related to the model through reduced frequency k that can be calculated with $k = \omega b/V$. Aerodynamic constants c_1-c_4 are derived with the Sears and Pade approximations [19]. The aerodynamic forces and structural matrices are integrated in the generalised form from Equation 2. With nonlinearity present in the pitch degree of freedom for the case studies under examination, the Boolean matrix allocating the nonlinear function is defined as $q_n = [0, 1, 0]^T$. The specific definition of the nonlinear function f_{nl} varies for each test case. This setup enables linear flutter analysis to precede the detailed numerical continuation method outlined.

To illustrate the nonlinear characteristics of the system under smooth nonlinear conditions, the spring stiffness is modelled using quadratic and cubic terms in the pitch degree of freedom. The shape of the smooth nonlinearity is demonstrated in Figure 3b. This method is commonly used to replicate geometrical nonlinear behaviours [34].

$$f_{nl}(t) = K_{\alpha 2}\alpha(t)^2 + K_{\alpha 3}\alpha(t)^3 \tag{29}$$

To capture the behaviour of a nonsmooth nonlinearity, the nonlinear function is now represented by a freeplay nonlinearity on the torsional spring, as depicted in Figure 3c. This describes behaviour where the torsional stiffness becomes zero within a range of pitch angles, typically denoted as $-\delta$ to δ, resulting in a nonsmooth shape. The segment with zero torsional stiffness is commonly referred to as the freeplay region. Functions of this type are typically employed to model nonlinear impacts arising from localised contact points and friction [1,5].

$$f_{nl}(t) = \begin{cases} K_{nl}(\alpha(t) + \delta) & \alpha(t) \leqslant -\delta \\ 0 & -\delta < \alpha(t) < \delta \\ K_{nl}(\alpha(t) - \delta) & \alpha(t) \geqslant \delta \end{cases} \tag{30}$$

4 Numerical demonstration and validation

In this section, the outlined methodology will be applied to the specified aeroelastic test case for a purely numerical validation assessment. This will involve comparing the accuracy of bifurcation diagrams to time histories and time-domain continuation tools, namely MATCONT and COCO. The examination will consider both precision and computational cost. Two distinct types of nonlinearity will be explored. Firstly, a smooth nonlinearity, typically employed to model geometric nonlinearities, will be analysed. Subsequently, a nonsmooth function will be utilised to represent localised nonlinearity.

4.1 Smooth nonlinearity

The results obtained by implementing the smooth nonlinearity described in Equation 29 are presented herein. To build the Hill's matrix for frequency domain stability analysis, $\frac{df_{nl}}{d\mathbf{x}}(t)$ is derived from Equation 29 as follows:

$$\frac{df_{nl}}{d\mathbf{x}}(t) = 2K_{\alpha 2}\alpha(t) + 3K_{\alpha 3}\alpha(t)^2 \tag{31}$$

The parameters outlined in Appendix A define the test case. For the purely numerical test, a simplified aerodynamic model is utilised, resulting in the neglect of the aerodynamic state w. Consequently, both structural and aerodynamic matrices (Equations 27 and 28) are reduced from 3×3 to 2×2.

The HBM framework was applied to the test case, and bifurcation diagrams for various harmonic orders are presented in Figure 4a. Continuation was initiated from the Hopf bifurcation point (flutter velocity) at 31.45 m/s, identified through linear eigenvalue analysis of the matrix Q. The continuation initially progressed backward with respect to velocity until reaching a turning point, after which the direction reversed. This is subcritcal behaviour, meaning LCO exist at lower velocities than the linear flutter speed.

To establish a reference solution, a high-fidelity run with 100 harmonics was conducted to assess the mean error in velocity for LCO amplitudes ranging from 0 to 0.5 rad. Figure 4b indicates that mean error relative to the 100-harmonic solution converges fully by five harmonics. It is observed that the error in the shape of the bifurcation curves for one and two harmonics is nearly identical, with a sharp change occurring at three harmonics. A steep 99.08% reduction in absolute error is observed between two and three harmonics, followed by only marginal decreases up to five harmonics. This trend is validated by Figure 4a, which shows a slight change in the bifurcation diagram's shape between two and three harmonics, with negligible differences beyond three harmonics.

From a design perspective, the turning point is critical as it represents the minimum velocity at which LCOs are expected. Figure 4c reveals a 1.42% change in the turning point location between two and three harmonics, with only minor variations up to five harmonics. While the steep error reduction

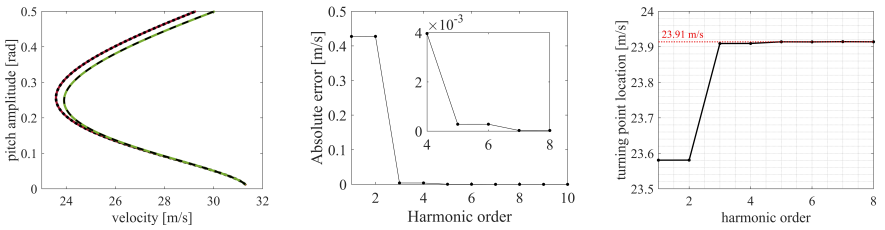

(a) (b) (c)

Fig. 4: Bifurcation diagram for smooth nonlineaity (a) Shape convergence ($\cdots$ $l = 1$), ($\bullet$ $l = 2$), ($\bullet$ $l = 3$), (-- $l = 100$), (b) Bifurcation diagram mean error, (c) Turning point convergence

between two and three harmonics has limited impact on the overall bifurcation diagram shape, full convergence is not achieved until five harmonics with a turning point at $23.91 m/s$.

The convergence of frequency-domain stability methods is assessed after the bifurcation diagram stabilises. Standard time-domain Floquet analysis, as shown in Figure 5a, serves as a reference for stability behaviour. For LCO amplitudes below $0.25 rad$, the Floquet multiplier associated with mode 4 exceeds unity, indicating unstable LCO behaviour. Conversely, for amplitudes exceeding $0.25 rad$, all Floquet multipliers are less than or equal to unity throughout the remainder of the continuation, signifying stable LCO. It is observed that the multiplier for mode 3 remains exactly 1 across the entire continuation. The stability exchange point corresponds to the turning point in the bifurcation diagram, occurring at a velocity of $23.91 m/s$. This indicates the presence of unstable LCOs at low amplitudes, spanning from the turning point to the Hopf bifurcation point. At the turning point, a stability exchange takes place, leading to the emergence of higher-amplitude stable LCOs.

While time integration provides an exact determination of LCO stability, converting to the time-domain undermines the purpose of employing a frequency domain method for delineating the shape of the bifurcation diagram. Therefore, stability is evaluated using both the standard Hill's method and the Koopman operator-based method to determine the optimal approach in this context, considering accuracy and runtime. Figure 5b shows the critical Floquet exponent obtained from the standard Hill's method at 5 Harmonics, indicating where a change of stability occurs. It is observed that the transition from stability to instability occurs within $0.01 m/s$ of the prediction made by the time-integration method. Similarly, in Figure 5c, the Koopman operator based method at 5 Harmonics predicts stability exchange at the same point as the standard Hill's method.

It is observed in Figure 5b that the Hill's method exhibits an anomalous jump in the Floquet exponent at the point of stability exchange. Furthermore, the Floquet multipliers derived from the Koopman method in Figure 5c do not align precisely with those obtained from direct time integration. This discrep-

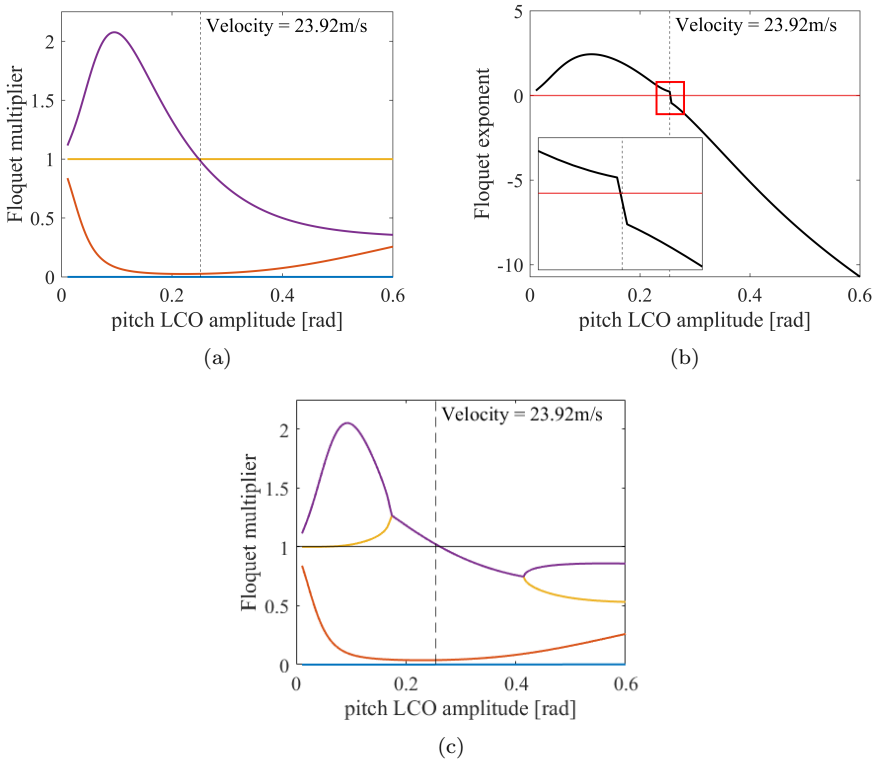

Fig. 5: Smooth nonlinearity stability eigenvalues a $l = 5$ (• eigenvalue 1), (• eigenvalue 2), (• eigenvalue 3), (• eigenvalue 4) (a) Time integration, (b) Standard Hill's method, (c) Koopman based method

ancy suggests that modes 3 and 4 are coupled near the stability exchange point but decouple thereafter. While the stability exchange is captured in this instance, further investigation is warranted to determine under what conditions, if any, these results converge to the exact solution.

Focusing initially on the Hill's method, since no exact solution is available for direct comparison, the harmonic order was increased to 100 to achieve fully converged Floquet exponents, as shown in Figure 6a. The resulting curve is smooth and exhibits no anomalous jumps near the stability exchange, indicating convergence. This solution is treated as the reference for evaluating the accuracy of Floquet exponents at lower harmonic orders. The mean error over the critical range of LCO amplitudes of interest is presented in Figure 6b. By six harmonic orders, the error is observed to converge, and this is further confirmed in Figure 6c, which demonstrates that for harmonic orders below six, a jump near the stability exchange is evident, whereas at six harmonics, the curve becomes smooth. Despite these jumps, the stability exchange location converges by five harmonic orders. An exception to this is the single

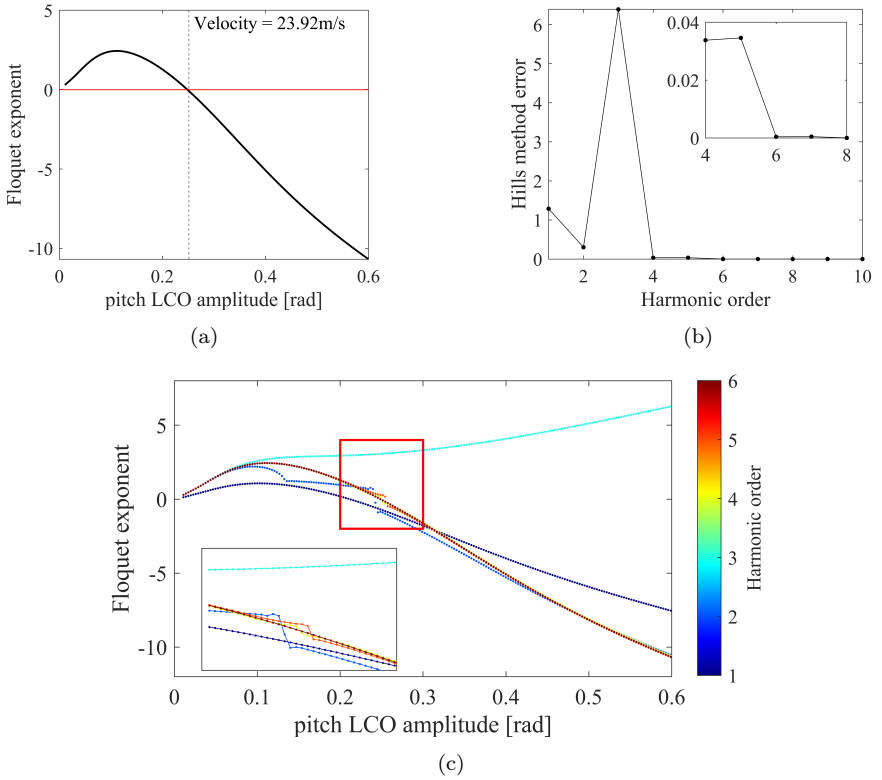

Fig. 6: Hill's stability method on smooth test case (a) Converged Floquet exponents, (b) Floquet exponent mean error, (c) Convergence study

harmonic response, where a smooth curve is observed. However, this result underestimates the true stability exchange location by 25%, as reflected in the mean absolute error, making it the second least accurate among the cases considered. A significant increase in error at three harmonics is also observed. Examination of Figure 6c reveals that at this harmonic order, the Floquet exponents fail to predict stability, diverging instead to a large positive value.

Using the Koopman method, the exact Floquet multipliers derived from the time integration method serve as a benchmark for assessing its accuracy. Figure 7a demonstrates that the mean error in the multipliers converges at eight harmonic orders. It is observed that while modes 1 and 2 converge by six harmonic orders, modes 3 and 4—critical for determining stability—do not converge until eight orders. This is corroborated in Figure 7c, which shows that modes 3 and 4 remain coupled prior to eight harmonics. Beyond this point, the Koopman method accurately captures the dynamics of modes 3 and 4, with mode 3 maintaining a multiplier of 1 throughout the bifurcation diagram, while mode 4 exhibits a smooth transition from stable to unstable.

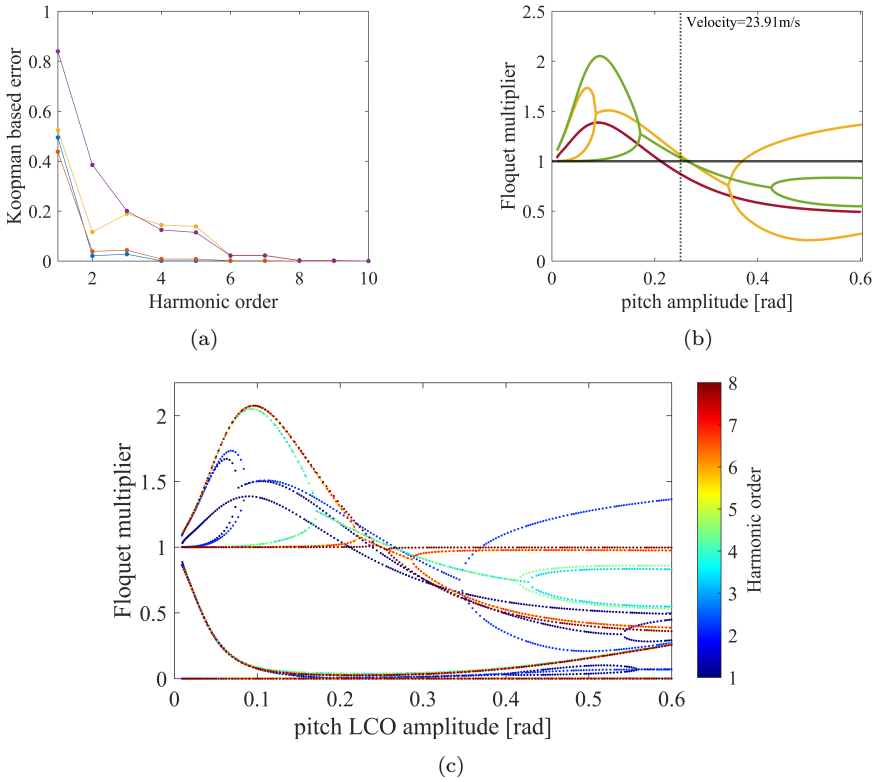

Fig. 7: Koopman-based stability on smooth test case (a) Floquet multiplier error (colours in line with Figure 5a), (b) Mode 3 and 4 coupling at (• $l = 1$), (• $l = 3$), (• $l = 5$), (c) Convergence study

Figure 7b highlights the multipliers for modes 3 and 4 at low harmonic orders, with the modes being fully coupled for the full continuation run in the single harmonic result. At harmonic orders between two and four, the stability transition location is underestimated. Notably, at three harmonic orders, the Koopman method predicts that the system becomes unstable again at higher amplitudes in the bifurcation diagram. However, despite discrepancies in the Floquet multiplier shape compared to the exact solution, the stability transition location converges to the value predicted by the time-domain method by five harmonic orders.

The final converged bifurcation diagram, shown in Figure 8, is generated using a harmonic order of 5 with Koopman-based stability analysis. The results reveal subcritical behaviour, where unstable LCOs are tracked from the linear flutter velocity up to 23.91 m/s. Beyond this point, a turning point is reached, after which stable LCOs of increasing amplitude are observed with rising velocity.

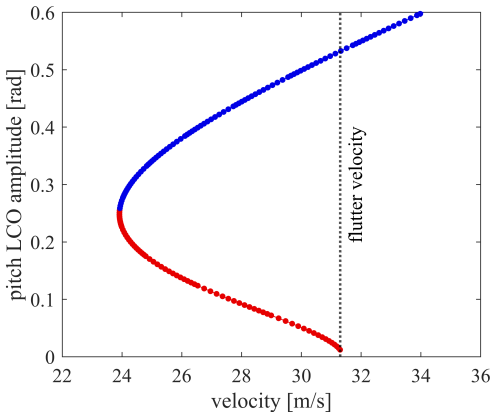

Fig. 8: Smooth test case converged bifurcation diagram at $l = 5$ (• unstable LCO), (• stable LCO)

4.2 Nonsmooth nonlinearity

The outcomes derived from applying the freeplay nonlinearity outlined in Equation 30 are presented in this section. To construct Hill's matrix for frequency domain stability analysis, $\frac{df_{nl}}{d\mathbf{x}}(t)$ is derived from Equation 30 as follows:

$$\frac{df_{nl}}{d\mathbf{x}}(t) = \begin{cases} K_{nl} & \alpha(t) \leqslant -\delta \\ 0 & -\delta < \alpha(t) < \delta \\ K_{nl} & \alpha(t) \geqslant \delta \end{cases} \tag{32}$$

The parameters are once again outlined in Appendix A, with the primary distinction being the incorporation of nonlinearity in the case of the localised nonlinearity. In the implemented freeplay nonlinearity, two distinct linear flutter velocities emerge. The first occurs when the absolute value of the pitch is less than δ, resulting in zero torsional stiffness. Under this condition, the flutter velocity remains consistent with the smooth case at $31.45m/s$ (flutter velocity 1). Conversely, in scenarios where $|\alpha| \geqslant \delta$, the flutter velocity is determined by setting $K_\alpha = K_{nl}$ and is calculated to be $29.5m/s$ (flutter velocity 2). Given that flutter velocity 1 corresponds to the hopf bifurcation point, continuation will commence from this point, assuming the aerofoil is perturbed from a state with zero heave and pitch.

Continuation is initiated from flutter velocity 1, and bifurcation diagrams are generated across a range of harmonic orders. The results obtained using 100 harmonic orders are taken as the reference for assessing convergence of the bifurcation diagram's shape. Figure 9a illustrates a subcritical pattern, similar to the smooth case, but with a sharper transition. Notably, LCO amplitudes remain negligible before the turning point, beyond which they escalate towards infinity.

Figure 9a further shows similarity between the single and two harmonic result and a noticeable change in the shape of the bifurcation curve at the turning point between 2 and 3 harmonics. However, for harmonic orders above 3, even up to 100, the changes are minimal. This observation is validated by the absolute error presented in Figure 9b, where a 78.41% drop in error relative to the 100-harmonic result is observed between 2 and 3 harmonics. An additional 17.26% reduction occurs between 3 and 5 harmonics, but beyond this, only marginal decreases are observed, with full convergence achieved around 10 harmonics.

As in the smooth case study, the turning point location remains the most critical feature of the bifurcation diagram. Figure 9c shows that significant jumps in absolute error result in only a 3.25% change in the turning point velocity between 2 and 3 harmonics, with minor adjustments thereafter. Convergence is reached at 8 harmonics, yielding a turning point velocity of 24.29 m/s. Although the bifurcation shape converges at 10 harmonics, it suggests that the amplitude also requires up to 10 harmonics to achieve full convergence.

Once the bifurcation diagram has stabilised with time integration Floquet analysis, as shown in Figure 5a as the reference point, the convergence of frequency domain stability methods is re-assessed. Given the minimal change in amplitude before the turning point in the bifurcation diagram, iteration along the continuation process replaces the LCO amplitude in the stability plots. Time-integration stability indicates an exchange from unstable to stable at iteration 44, corresponding to the turning point of the bifurcation diagram.

Upon examination of the Floquet multipliers and exponents of the frequency domain methods in Figures 10b and 10c, an erratic pattern is noticeable, with sharp jumps between points. This contrast with the time-domain method suggests discrepancies in depicting the dynamic behaviour. However, in the case of standard Hill's method, such behaviour does not influence the prediction of stability exchange. Despite the erratic nature of the critical Floquet exponent, it still indicates the transition of LCO from unstable to stable at iteration 44, as shown in Figure 10b.

As there is no exact solution for the Floquet exponents, the result obtained using 100 harmonic orders, shown in Figure 11a, is adopted as the converged solution for accuracy assessment. This plot reveals a generally smooth curve, particularly near the stability exchange point. The mean error in the Floquet exponents over the full continuation run is illustrated in Figure 11b. It is observed that the error begins to converge at harmonic orders exceeding 15.

In the outputs from the Hill's method, erratic jumps are consistently observed. However, as shown in Figure 11c, for harmonic orders above four, all Floquet exponents correctly predict an exchange of stability at iteration 44, aligning with the time-domain results. Once again, the single harmonic result exhibits a smooth curve across all iterations but underestimates the turning point location by 12 iterations. Any Floquet multipliers appearing in the top-right or bottom-left quadrants of Figure 11c indicate an error. Notably, such erroneous points are confined to results at harmonic orders below five. This indicates that, despite the chaotic appearance of the results at low harmonic

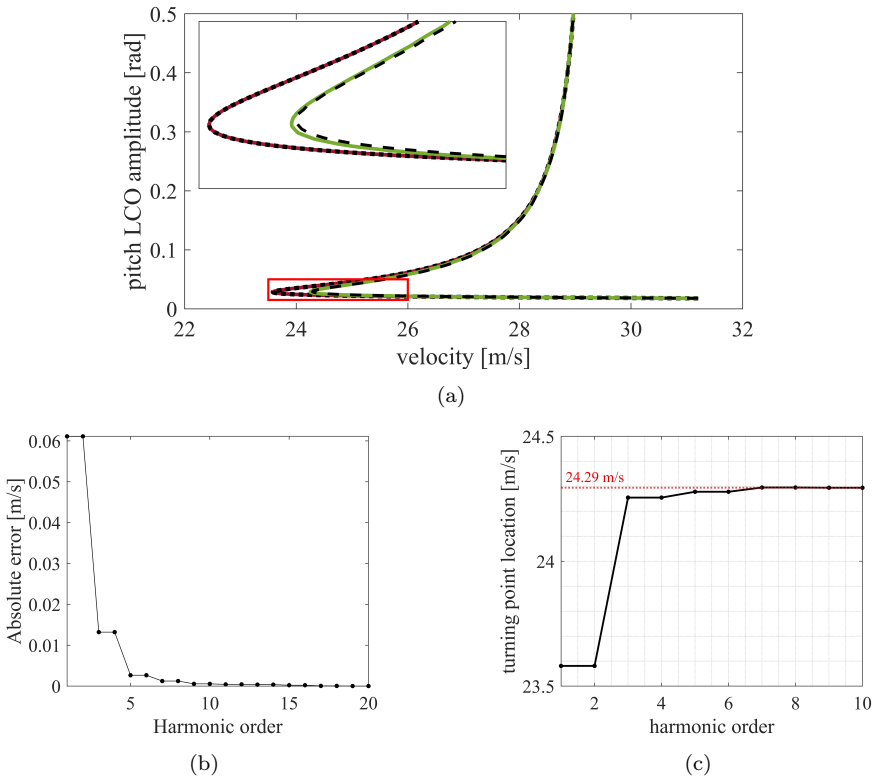

Fig. 9: Freeplay bifurcation diagram (a) ($\cdots$ $l = 1$), ($\bullet$ $l = 2$), ($\bullet$ $l = 4$), ($\bullet$ $l = 8$), (b) Bifurcation diagram absolute error, (c) Turning point loaction convergence

orders, meaningful stability information can still be extracted. Consequently, reliable stability predictions can be obtained even at relatively low harmonic orders, provided the analysis is carefully interpreted.

Focusing on the results from the Koopman-based method, the apparent errors in the Floquet multipliers obtained through Koopman operator-based stability analysis significantly influence the outcomes. A detailed examination of the critical multipliers in Figure 10c reveals that eigenvalues 3 and 4 exhibit chaotic jumps between iterations. Unlike the Floquet exponents, chaotic transitions between stable and unstable states are observed following the exchange of stability indicated by the time-domain results. Additionally, the modes appear to be coupled near the stability exchange point, which contrasts with the time-domain results where mode 4 consistently remains at 1 throughout the continuation. This erratic behaviour is illustrated in Figure 12a, where the bifurcation diagram shows unpredictable shifts between stability and instability after the turning point. These deviations are inconsistent with the more

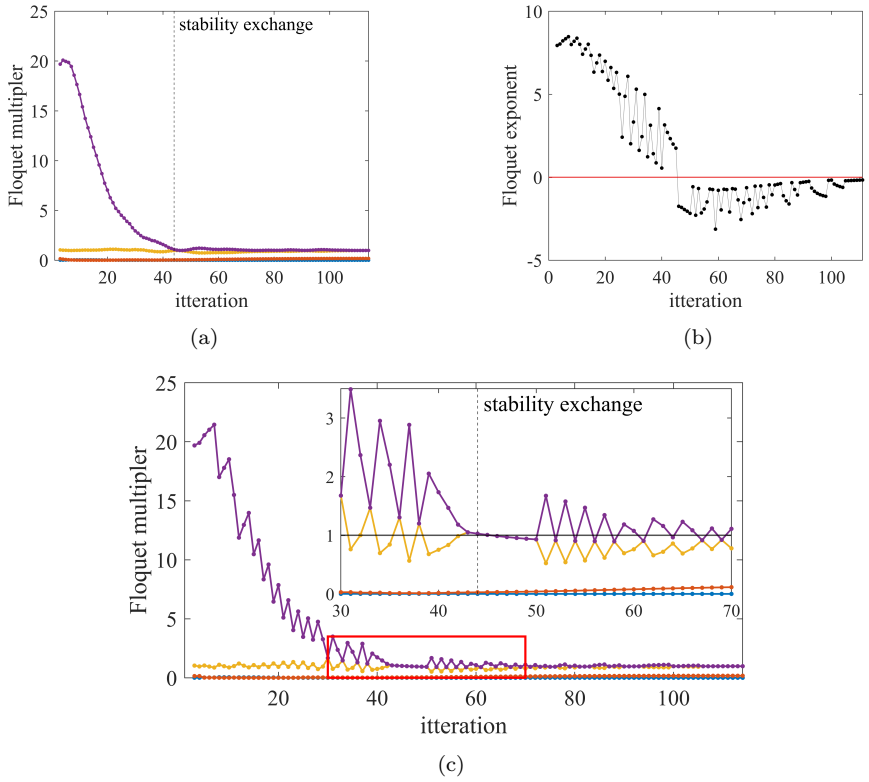

Fig. 10: Freeplay nonlinearity stability eigenvalues at $l = 8$ (• eigenvalue 1), (• eigenvalue 2), (• eigenvalue 3), (• eigenvalue 4) (a) Time integration, (b) Standard Hill's method, (c) Koopman operator based stability

reliable predictions derived from the time-integration method. An exception is observed in the single harmonic case, where the Floquet multiplier curve remains smooth throughout the continuation, with no chaotic jumps. However, this result yields the largest error compared to the time-domain solution, underestimating the stability exchange by 12 iterations.

The error in the Floquet multipliers from the Koopman method is evaluated against the exact solution obtained from the time integration method. Figure 12b indicates that while the errors for all modes begin to converge at 20 harmonic orders, they remain relatively high for the critical modes 3 and 4, which govern the stability of the LCO. Figure 12c confirms this observation, demonstrating that although the general shape of the Floquet multipliers converges, chaotic jumps persist between iterations, along with incorrect stability transitions where none should exist. Notably, if any Floquet multipliers fall within the top-right quadrant of Figure 12c, this indicates an error. The presence of multiple erroneous points, not limited to regions near the stability

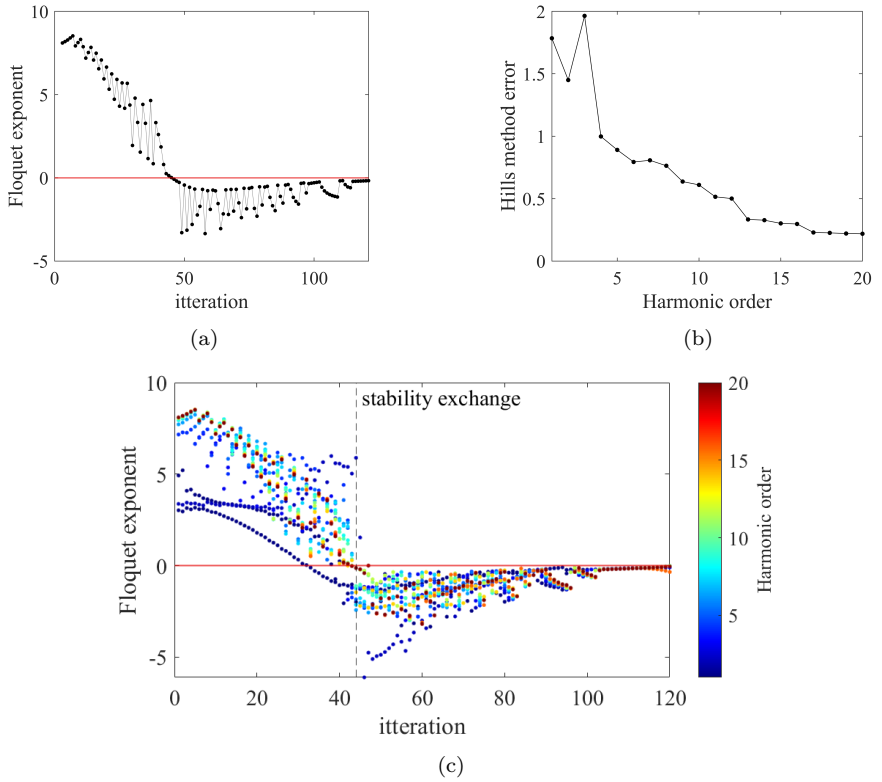

Fig. 11: Hill's stability method on nonsmooth test case (a) Converged Floquet exponents, (b) Floquet exponent mean error, (c) Convergence study

exchange, highlights a broader issue. Even at 100 harmonic orders, chaotic jumps in stability persist, suggesting that the Koopman operator, as applied in this problem, cannot fully capture the stability of the non-smooth case.

The presence of errors in the Hill and Koopman stability methods may be attributed to the inherent approximation nature of the harmonic balance method in capturing the dynamic behaviour of a system. In essence, frequency domain methods can only be as effective as their ability to estimate true time histories accurately. This notion is underscored by comparing the true time histories of nonlinear forces with the frequency domain estimates obtained through the AFT procedure, as depicted in Figure 13.

An analysis of the error in the case of smooth nonlinearity, presented in Figures 13a and 13b, reveal that the AFT procedure offers a reasonable approximation of the true nonlinear force at both low and high LCO amplitudes. The relative root mean square error (RRMS) remains below 10^{-3} in both instances, explaining why both frequency domain stability methods exhibit success without chaotic jumps between iterations.

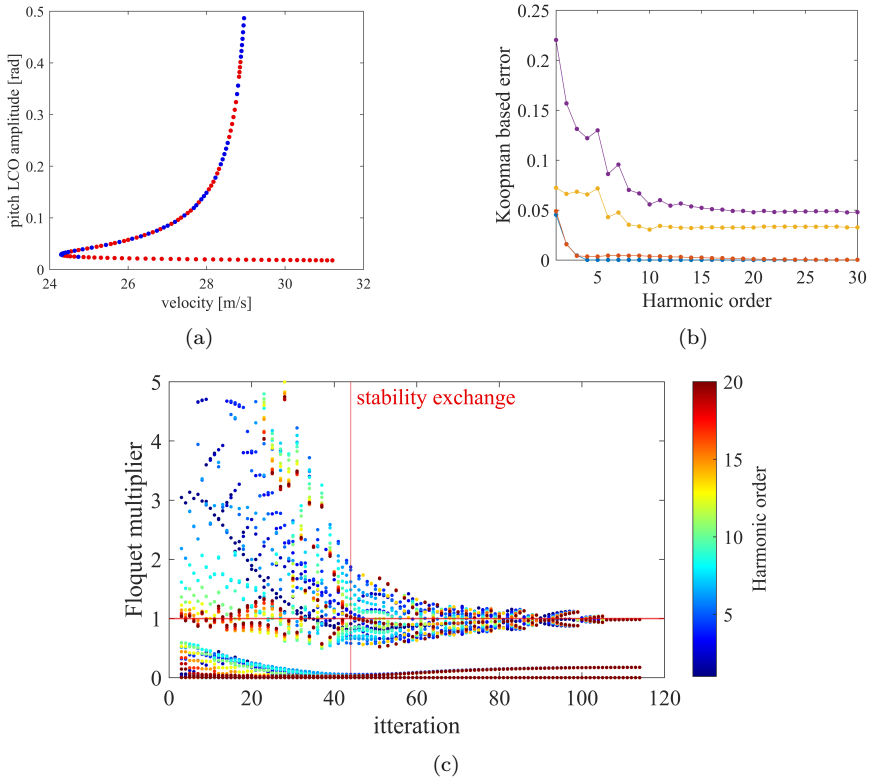

Fig. 12: Koopman-based stability on smooth test case (a) Bifurcation diagram with stability $l = 8$ (• unstable LCO), (• stable LCO), (b) Floquet multiplier error (colours in line with Figure 10c), (c) Convergence study

However, when examining the case of a nonsmooth freeplay nonlinearity, as shown in Figures 13c and 13d, the AFT procedure struggles to accurately capture the behaviour of the nonlinear force. Particularly at low LCO amplitudes, where the freeplay region induces a sharp transition of the nonlinear force to zero, the frequency domain method fails to replicate this flat-line behaviour. Consequently, there is an underestimation in the peak of the force. The RRMS error at low LCO amplitude is five orders of magnitude higher than in the smooth case. Although this error diminishes as LCO amplitude increases and the freeplay region becomes less influential, the mean RRMS error remains two orders of magnitude larger than in the smooth case. This error source is akin to the Gibbs phenomenon, which states that the error will diminish as the number of harmonics increases but will always be present to some degree [25,10]. The discrepancy likely elucidates the erratic nature of the frequency domain estimations of stability for the nonsmooth case.

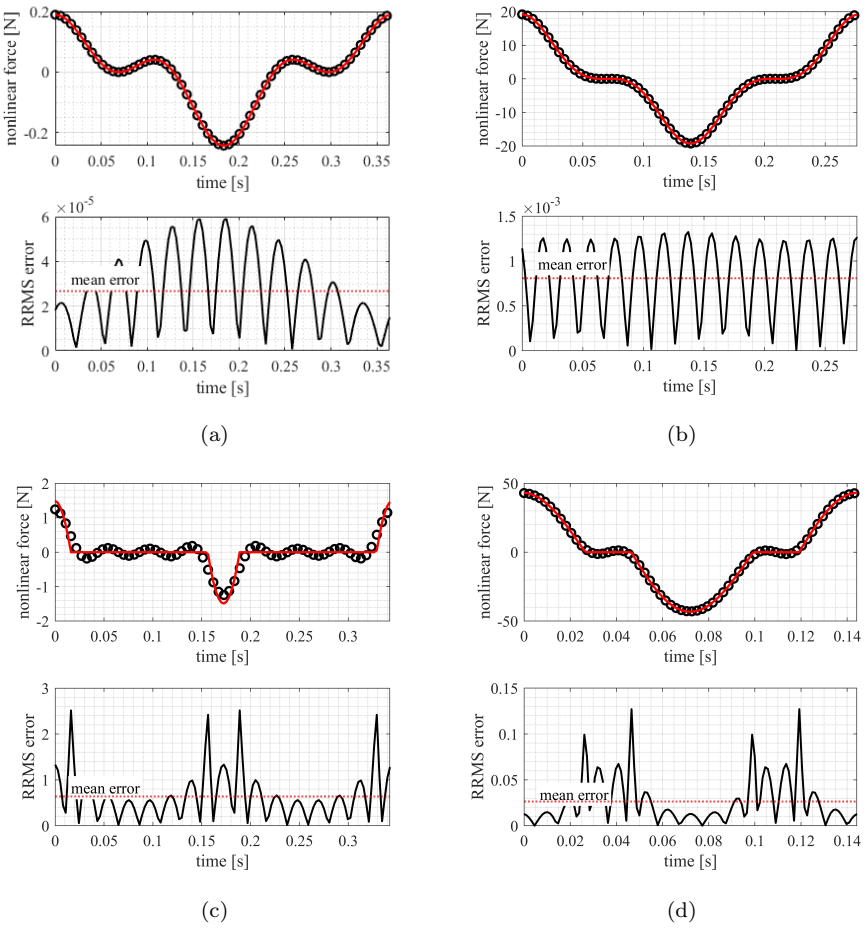

Fig. 13: AFT error (– nonlinear force response), (⊖ AFT estimation), Smooth: (a) LCO amplitude = $0.02rad$, (b) LCO amplitude = $0.20rad$, Nonsmooth: (c) LCO amplitude = $0.02rad$, (d) LCO amplitude = $0.20rad$

An alternative explanation for the jumps observed in the Koopman operators may lie in the continuous nature of the oscillatory nonlinear force, f_{nl}, despite its discontinuous slope. The erratic patterns evident in Figures 10b and 10c could initially be interpreted as reminiscent of the Gibbs phenomenon. However, they are more likely attributable to the jump discontinuities in the Jacobian of f_{nl}. These discontinuities can induce abrupt variations in the system's response, particularly in regions of heightened sensitivity, resulting in the irregular behaviour observed in the results. This differentiation underscores the necessity of distinguishing numerical artefacts, such as the Gibbs phenomenon,

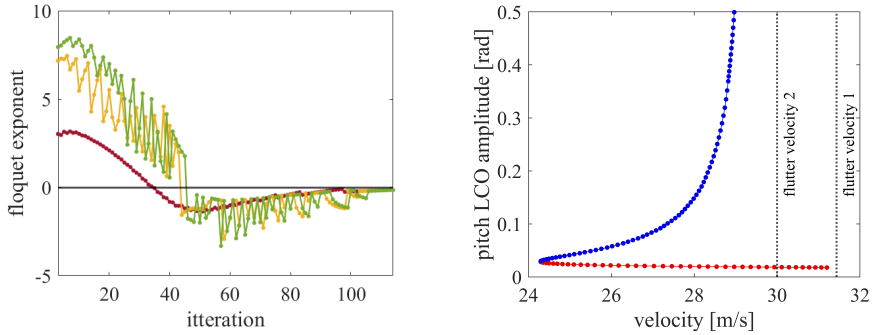

(a) (b)

Fig. 14: Nonsmooth nonlinearity study converged solution (a) Standard Hill's critical Floquet exponent (• $l = 1$), (• $l = 4$), (• $l = 8$), (b) Bifurcation diagram with sorted Hill stability (• unstable LCO), (• stable LCO)

from the inherent physical effects arising from nonlinear system properties, to facilitate a precise interpretation of stability and dynamic behaviour.

The stability information obtained from the standard Hill's method is employed to evaluate the stability of the bifurcation diagram in Figure 14b, which is considered the fully converged bifurcation plot for the freeplay study and will be compared to time-domain solvers in Section 4.4. Unstable LCOs are initiated at the bifurcation point (flutter velocity 1) and persist in reverse with respect to velocity until reaching $24.3m/s$. Subsequently, a turning point is encountered, resulting in an exchange of stability. Stable LCOs of growing amplitude then emerge between $24.3m/s$ and $29.5m/s$ (flutter velocity 2). At $29.5m/s$, flutter behaviour manifests, characterised by LCO amplitudes tending towards infinity.

4.3 Time domain comparison

Figure 15 compares converged bifurcation diagrams with time histories obtained from the MATLAB *ode*45 differential equation solver for both test cases. The smooth comparison in Figure 15a, not only clarifies the physical significance of the LCO plot but also validates its accuracy. At velocities below the turning point, the system responds to any initial perturbation in pitch or plunge by oscillating with positive damping before eventually settling to a steady rest state at zero. Responses within the velocity range between the turning point and the linear flutter speed vary depending on the magnitude of the initial perturbation. Small perturbations exhibit behaviour similar to those observed below the turning point, while larger perturbations lead to the generation of LCO. Beyond the linear flutter speed of $31.45m/s$, it is observed that the time response to any perturbation is an LCO with amplitude correlating to the bifurcation diagram.

Similar conclusions can be drawn from the non-smooth comparison in Figure 15b. Prior to the turning point, the system responds to any perturbation with a stable rest response. Between the turning point and flutter speed 2 $(24.3 - 29.5m/s)$, both stable and unstable LCO branches exist. This implies that under low perturbations, the system responds with a rest solution, while higher perturbations lead to stable LCO and is vaildated by time responses. The amplitude of LCO increases rapidly towards flutter speed 2, as depicted in both the time histories and the bifurcation diagram. Beyond velocities ranging from $29.5m/s$ to $31.45m/s$, the LCO plot indicates unstable LCOs, which either converge to a stable solution or diverge towards infinity. This observation is confirmed by the time responses, where systems settle with low perturbations but exhibit dynamic instability with larger ones (as shown in Figure 15). Above the linear flutter speed without torsional stiffness, both the LCO plot and the time histories indicate the absence of stable solutions, with the response to any perturbation resulting in binary flutter.

The comparison in Figure 15 illustrates that the peak points of the time responses accurately align with the stable curve generated from the HBM results in both test cases. It is worth noting that the amplitude of the unstable section of the LCO plot lacks physical significance. However, the plot clearly indicates that solutions lie on either side of the branch, resulting in either a steady-state rest or a vibrational response (flutter or LCO).

4.4 Software comparison

In this section, the converged HBM smooth and nonsmooth studies will be compared to time-domain solvers, considering both accuracy and computational cost. Bifurcation diagrams of the same systems are generated using state-of-the-art time-domain solvers, namely MATCONT and COCO. The bifurcation diagrams produced by these time-domain solvers yield identical results since both utilise time integration to establish their residual equations. The primary distinction between the two lies in their methods for setting up the residual equations: COCO employs orthogonal collocation, whereas MATCONT uses the standard method [15,12]. When comparing the HBM continuation results to those obtained from MATCONT and COCO, a high level of accuracy is evident. Figures 16 and 17 demonstrate the accurate prediction of stable LCO amplitude. It should also be noted that both MATCONT and COCO predict an exchange in stability in the turning points of both diagrams.

Considering the smooth nonlinearity test case, Figure 16 demonstrates almost identical agreement with the MATCONT/COCO bifurcation diagrams. Examining the RRMS error in Figure 16b, it is observed that the mean error appears essentially as noise and can be almost neglected. From this, we can assert that in the case of the smooth nonlinearity, the HBM framework provides adequate estimations of LCO behaviour.

Examining the freeplay comparison in Figure 17, inaccuracies in the amplitude of the unstable region are shown, as illustrated in Figure 17b. At the

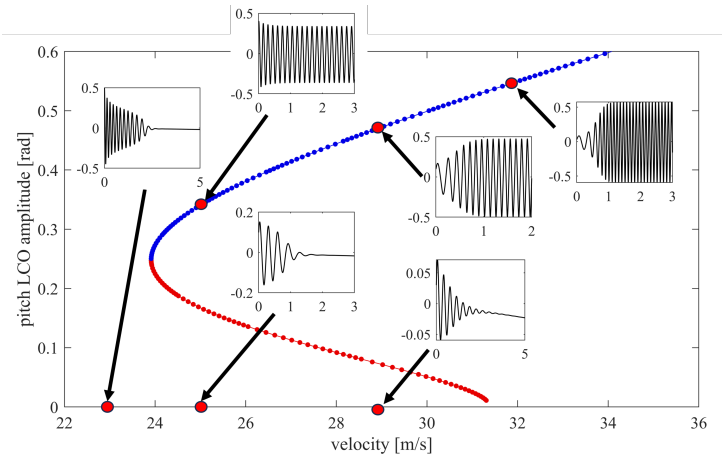

(a)

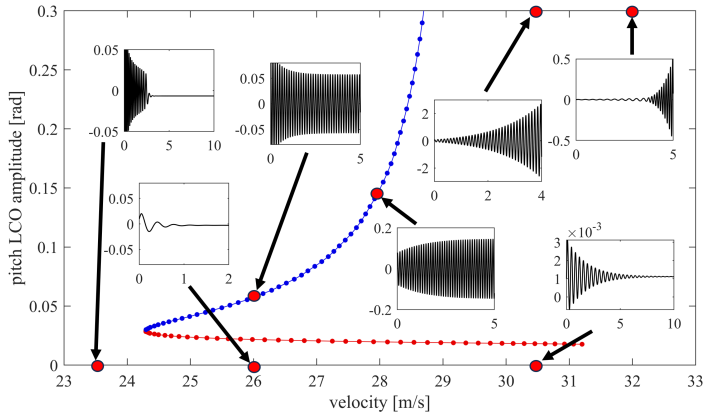

(b)

Fig. 15: Comparison of bifurcation diagram with time histories (• unstable LCO), (• stable LCO), (− pitch time history) (a) Smooth case, (b) Nonsmooth case

hopf point, the amplitude error measures at 45.71%. However, by iteration 30 ($27m/s$), the datasets align. This error may yet again be attributed to the Gibbs phenomenon described in Figure 13. As demonstrated in Figure 13d, at pitch LCO amplitudes of 0.10 rad, the mean RRMS error of the nonlinear force response is 27 times less than at 0.02 rad amplitude. This explains why prominent errors are observed at low LCO amplitudes but become less impactful at higher LCO amplitudes. Another potential explanation may relate to the freeplay gap. Specifically, when the LCO amplitude approaches the magnitude of the freeplay gap, the higher harmonic content in the nonlinear force becomes significantly amplified [44]. This phenomenon, as illustrated in

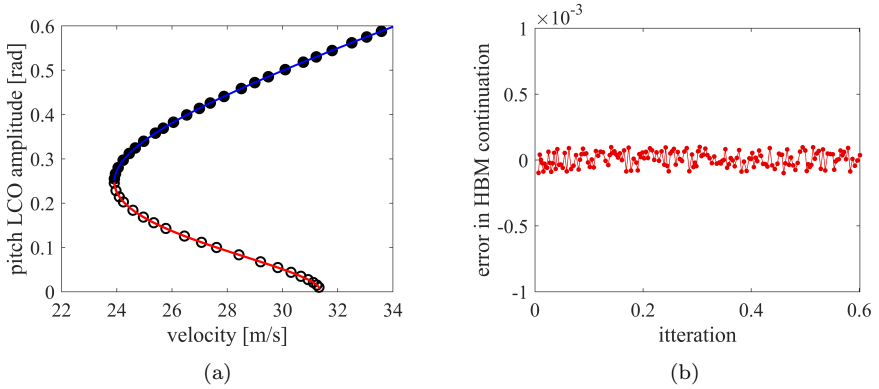

(a) (b)

Fig. 16: HBM continuation compared to time domain solvers for smooth nonlinearity (a) Bifurcation diagrm (HBM continuation: stable •, unstable **o**), (MATCONT/COCO: stable −, unstable −), (b) RMS error of HBM w.r.t MATCONT/COCO

Figure 13c, can contribute to irregularities in the system response, resulting in the erratic patterns observed in the results.

Regardless of the underlying cause of the error, no quantitative correlation was identified between the magnitude of the unstable LCO and the boundary at which perturbations settle to rest or transition to the stable LCO branch, as is observed in some systems. Instead, the unstable section of the bifurcation diagram offers more of a qualitative insight into the system's behaviour. Specifically, it demonstrated that for small perturbations, the system tends to settle to rest, whereas larger perturbations result in a stable LCO response, with amplitudes aligning with the stable section of the bifurcation diagram. Given that the LCO amplitude is accurately captured within the stable region of the bifurcation diagram, it can be argued that the HBM framework provides an acceptable representation of the dynamic system's physical behaviour in this case.

Considering the computational costs of the methods, the most computationally demanding aspect of each process involves generating a time series through numerical integration for time-domain methods and employing the AFT procedure for HBM continuation. This difference stands out as the primary distinction between the methods, while other steps remain consistent. In Figure 18a, we compare the computation time at an arbitrary point in the continuation for a single run of the AFT procedure with a time-integration solution covering a full period. It becomes evident that at harmonic orders below 9, the HBM continuation scheme is expected to exhibit lower computation times at a fundamental level. However, this assessment does not account for the frequency of iterations required before the convergence of residual equations is achieved, potentially undermining the apparent advantage of a full continuation run.

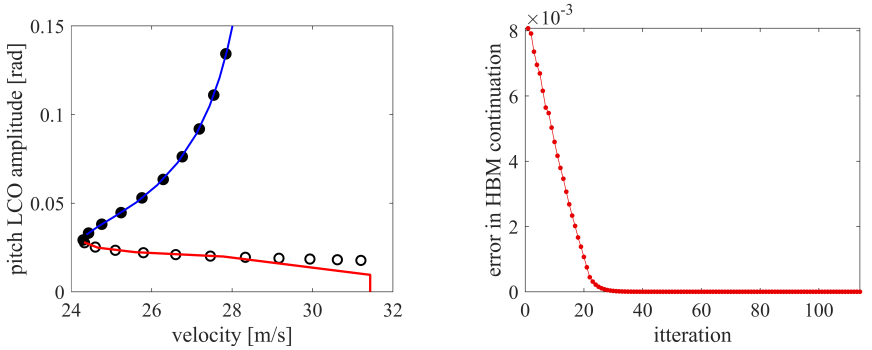

(a) (b)

Fig. 17: HBM continuation compared to time domain solvers for nonsmooth nonlinearity (a) Bifurcation diagrm (HBM continuation: stable •, unstable **o**), (MATCONT/COCO: stable −, unstable −), (b) RMS error of HBM w.r.t MATCONT/COCO

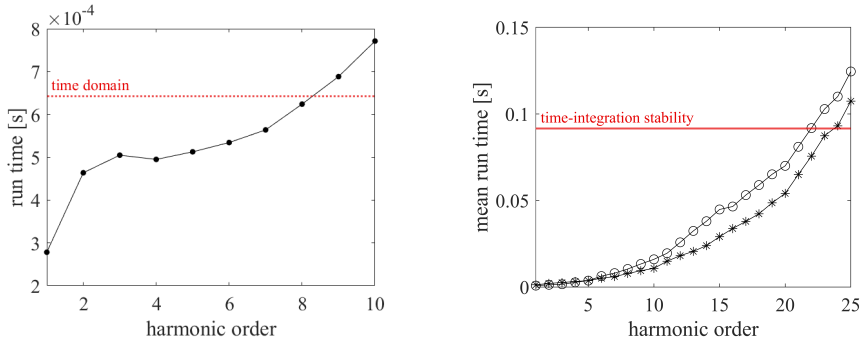

(a) (b)

Fig. 18: (a) Mean AFT method run time, (b) Stability method mean run time (⊖ standard Hill's),(∗ Koopman operator based stability)

An essential consideration when evaluating computational efficiency is the choice of stability analysis method. Figure 18b presents a comparison of the mean computational time for the three stability methods applied to a two-degree-of-freedom system, representative of both the smooth and nonsmooth cases studied in this work. A key observation is that both frequency-domain methods exhibit lower computational costs than standard time integration up to 22 harmonics. At lower harmonic orders, the computational costs of the two frequency-domain methods are comparable, with the standard Hill's method being slightly more efficient. However, at 5 harmonics, the Koopman operator-based method becomes less computationally expensive and retains this advantage at higher harmonics.

In the smooth test case, the bifurcation curve shape and the absolute error in the Hill's method have converged by 5 harmonics. Similarly, the Koopman method provides accurate stability predictions by this point. Given that stability prediction is the primary goal, and the Koopman method offers a 7% reduction in run time compared to Hill's method and a significant 90% reduction relative to time integration, the Koopman operator-based method emerges as the preferred approach for computational efficiency in smooth cases.

For the nonsmooth study, both the bifurcation diagram shape and error in the stability methods converge by 15 harmonics, making the Koopman method the optimal choice regarding computational time. However, as previously discussed, the Koopman method was unable to consistently predict the correct stability behaviour even after convergence. Despite the existence of errors relative to the fully converged solution, accurate conclusions about stability can be drawn by 8 harmonics. Therefore, the Hill's method at 8 harmonics is the optimal choice in this scenario, offering an 84.21% reduction in computational time compared to time integration while providing reliable stability predictions for the LCO.

Table 1 provides a comparison of the converged HBM solutions for both smooth and nonsmooth case studies to MATCONT and COCO, considering run-time and data storage requirements. This comparison is carried out over a full continuation run with 100 iterations. Regarding run-time, a similar pattern is observed for both the smooth and nonsmooth case studies. MATCONT is the slowest performing of the methods, while the HBM framework is the fastest. The HBM framework offers over a 90% reduction in run-time compared to MATCONT in both cases. For COCO, over a 60% reduction in time was observed in both cases with the converged HBM solutions. For all methods, the smooth case has a lower run-time than the nonsmooth. In the case of MATCONT/COCO, this is likely due to a higher number of time intervals being required to accurately capture the time behavior of the nonlinear force. For the HBM scheme, this is for two reasons: 5 harmonic orders were used in the converged smooth case, but 8 were used in the nonsmooth case, and the standard Hill's method was used over the Koopman operator based method for stability in the nonsmooth case.

Data storage refers to the amount of data stored to describe LCO behaviors over the full run. For the time domain methods, this includes the position points of each degree of freedom and time steps obtained through numerical integration. The method of discretion of time steps differs slightly between MATCONT and COCO. In MATCONT, a set tolerance is automatically calculated at each run and used to set a constant time interval over a full period. In COCO, a variable time step is automatically computed as the time-integration is carried out over a period. In the HBM framework, the required data includes the Fourier coefficients describing each degree of freedom's amplitude and natural frequency. Fourier coefficients of the nonlinear force and nonlinear force differential are also required to compute stability. It appears there is a direct relationship between data storage requirements and run time, as more data is required to be handled, resulting in higher run times. The same conclusions

are then reached from looking at the data storage and run time comparisons. With the considered test case, below 32 harmonics, HBM is more data efficient than COCO in the smooth case and below 44 in the nonsmooth case.

Table 1: HBM time and data storage requirement comparison to generate full bifurcation diagram

	smooth		nonsmooth	
Software	Run Time [s]	Data Storage	Run Time [s]	Data Storage
MATCONT	105.78	46200	145.31	64600
COCO	29.44	38645	34.16	53250
HBM	10.40	6800	12.68	10400

From the comparisons of both accuracy and computational cost of the HBM framework to MATCONT and COCO, it is evident that the HBM framework is more effective at estimating LCO behaviour via bifurcation diagrams in both the smooth and nonsmooth test cases. However, it should be mentioned that a key reason for this, particularly considering computational cost, is due to the capabilities of each tool. Both MATCONT and COCO have capabilities for searching for other types of bifurcations, and particularly in the case of MATCONT, they provide a more in-depth user interface. In contrast, the proposed HBM framework is only suited for generating bifurcation diagrams to describe LCO behaviour.

5 Experimental study and validation

Having validated the HBM framework in a purely numerical test in the previous section, the subsequent section aims to experimentally validate it. Experimental LCO data for two different configurations will be compared with predictions from the HBM framework.

5.1 Experimental test rig

Pre-existing experimental data collected at the University of Bristol by Lee et al. [34] has been utilised to validate the methods proposed in this study. Figure 19 illustrates the experimental flutter rig, consisting of a NACA-0015 wing profile firmly affixed to a stainless steel shaft. The aerofoil is supported by rotational bearings on each end, enabling rotation, along with a bearing system facilitating vertical displacement. The spring in the heave degree of freedom behaves linearly. Additionally, leaf springs are introduced in the bearings to induce a nonlinear hardening effect in pitch motion. This setup replicates nonlinear effects encountered at interfaces in real aircraft. Further details of the setup can be found in Ref [33]. Heave displacement is measured using an Omron ZX1-LD300 laser displacement sensor, while pitch motion is captured by an

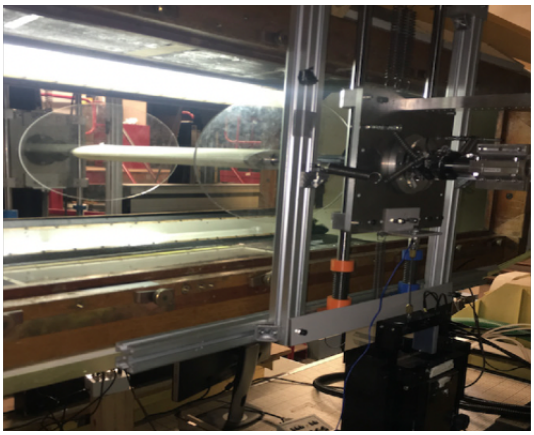

Fig. 19: The wing aerofoil flutter rig experimental configuration taken from [57]

RLS AksIM 18-bit absolute magnetic encoder. Wind speed is directly recorded from the wind tunnel control system. Stable and unstable LCO are captured through control-based continuation (see Ref [7] for a deeper explanation on CBC and its application in this context). The raw data undergoes fast Fourier transform analysis to minimise noise, a process repeated for two experimental configurations with different spring constants. Design rig parameters for each configuration are displayed in Table 2.

5.2 Numerical modeling

The linear mathematical model described in Equations 27 and 28 is once again utilised. In this test, however, the aerodynamic state w is introduced as a degree of freedom to create a more intricate aerodynamic model. Consequently, the full 3×3 structural and aerodynamic matrices are employed to construct the Q matrix. As the leaf spring employed in the experimental setup was intended to replicate the behaviour of a geometric nonlinearity, the smooth nonlinearity from Equation 29 is again applied to the pitch degree of freedom.

The parameters outlined in Table 2 are determined for both experimental configurations. Flutter speeds for each setup are obtained through eigenvalue analysis, as also depicted in the table. Estimates for the nonlinear parameters $K_{\alpha 2}$ and $K_{\alpha 3}$ are required. Here, deterministic estimates derived from normal theory, as found in the original study [34],as well as updated estimates obtained from a probabilistic data-driven Bayesian approach, are separately employed [40].

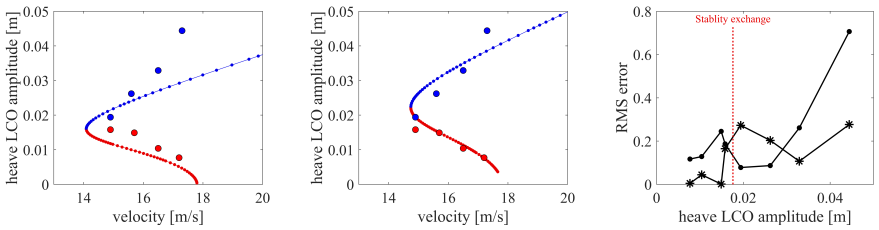

(a) (b) (c)

Fig. 20: Experimental configuration 1: (a) With deterministic parameter estimate at $l = 5$, (b) With probabilistic parameter estimate at $l = 5$, (c) Error w.r.t CBC data [34] (• deterministic), (* probabilistic). Note: • stable LCO; • unstable LCO

5.3 Comparsions between numerical and experimental results

The converged HBM continuation results, employing parameters for both experimental configurations, are now compared with the CBC data to assess the accuracy of both LCO amplitude and stability. The comparison with configuration 1 is depicted in Figure 20 for both deterministic and probabilistic parameter estimates. Both the HBM continuation plots and the experimental data exhibit a similar shape, featuring unstable LCO formations preceding a turning point, followed by stable LCO formations. However, discrepancies are evident in the amplitude of the plots, particularly in the deterministic estimate. Figure 20c illustrates that errors in amplitude become more pronounced as the amplitude increases in the stable section of the bifurcation diagram, with the highest amplitude point deviating significantly from the bifurcation plot in both estimates. It appears that the gradient of the bifurcation plot aligns with the experimental data before the turning point, but subsequently underestimates the gradient of the experimental data, particularly in the deterministic estimate. Overall, the probabilistic estimate provides a better approximation of the experimental data, with a mean RMS error of 0.13 compared to 0.23 in the deterministic case.

The comparison with configuration 2 is illustrated in Figure 21. Similar to configuration 1, both the HBM continuation results and the CBC data exhibit unstable LCO at low amplitudes until a turning point is reached, after which stable LCO begin to form. Both sets of HBM results adeptly capture the shape of the unstable section of the bifurcation diagram, showcasing low RMS errors below 15%, as indicated in Figure 21c. However, following the turning point, the shape of the bifurcation diagrams diverges from the CBC data, displaying a shallower gradient than expected, particularly in the deterministic estimate. Additionally, in the deterministic estimate, it appears that the location of the turning point is overestimated, extending back in velocity further than anticipated. This is not the case in the probabilistic estimate, where it appears the location of the turning point has been estimated more accurately. Again,

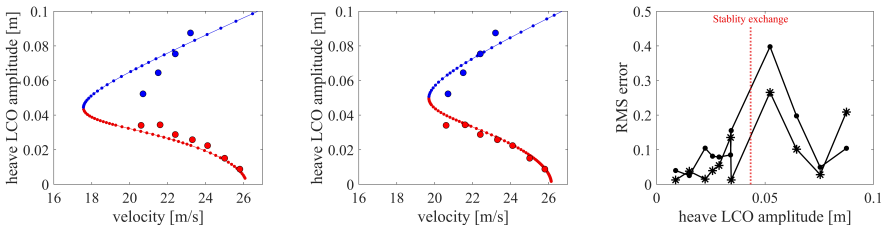

(a) (b) (c)

Fig. 21: Experimental configuration 2: (a) With deterministic parameter estimate at $l = 5$, (b) With probabilistic parameter estimate at $l = 5$, (c) Error w.r.t CBC data [34] (• deterministic), (* probabilistic). Note: • stable LCO; • unstable LCO

it is observed that the probabilistic estimate captures the behaviour of the data more closely. The probabilistic estimate has a mean RMS error of 0.083 compared to the higher 0.12 in the deterministic case. This is likely due to the probabilistic approach accounting for parameter uncertainties, thereby providing a more robust prediction of system behaviour across varying conditions. This enhances accuracy compared to the deterministic method [40]. In either case, both estimates provide an improvement over the estimated bifurcation diagrams in configuration 1. Consequently, it can be argued that the HBM continuation scheme captures the real behaviour in configuration 2, particularly with the probabilistic estimate.

Overall, the comparison between the HBM continuation scheme and CBC data in this case study presents a mixed outcome. In each configuration, the general shape of the bifurcation diagram is accurate, depicting a subcritical plot with unstable LCO at low amplitudes and stable LCO after the turning point. At low amplitudes, the RMS errors were relatively low, particularly in the second configuration; however, substantial errors are observed after the turning point. In both configurations, it appears that the gradient of the bifurcation diagram is lower than expected, leading to more pronounced errors at higher LCO amplitudes. This discrepancy suggests a potential issue with either the experimental data, the mathematical model, or the estimated parameters. Improvements in accuracy are, however, observed with the probabilistic parameter estimates over the deterministic ones, especially in configuration 2, where the completed bifurcation diagram has a mean RMS error under 10%.

6 Conclusion

This study proposed a computationally efficient method for estimating Limit Cycle Oscillation behaviour and determining stability in aeroelastic systems. The methodology involved conducting LCO analysis solely in the frequency do-

main, integrating the Harmonic Balance Method continuation and the Koopman operator.

The paper elucidated the methodology for a general aeroelastic frequency domain solver for LCO, providing detailed insights into the HBM continuation scheme and frequency domain stability analysis. Subsequently, this methodology was put into practice through a numerical test case, encompassing both geometric and localised nonlinearities. The results were validated against outcomes from MATCONT and COCO, with additional comparison against LCO experimental data obtained through Control Based Continuation experiments.

In the smooth nonlinear numerical test, successful convergence of bifurcation diagrams and LCO stability estimation was achieved at 5 harmonic orders. The Koopman operator-based method emerged as the preferred choice for stability analysis, offering notable reductions in run-time compared to standard Hill's method and time integration. However, in the nonsmooth nonlinear numerical test, convergence of the bifurcation diagram was achieved at 8 harmonic orders. While the standard Hill's method proved successful compared to time-integration, the Koopman operator-based method exhibited chaotic behavior, rendering it unreliable for LCO stability determination.

Comparisons with MATCONT and COCO underscored the HBM framework's superiority in accuracy and computational efficiency, particularly evident in the smooth test case. Despite some discrepancies in the nonsmooth case, the HBM framework provided a satisfactory description of the system's dynamic behaviour.

The experimental validation against experimental data yielded mixed results, with an accurate depiction of bifurcation diagram shapes but notable errors observed after the turning point. However, improvements in accuracy were noted with probabilistic parameter estimates over deterministic ones, particularly in configuration 2.

Future research should focus on validating the proposed framework for more complex, higher-degree-of-freedom systems to establish its robustness and applicability. Emphasis should also be placed on demonstrating its potential advantages in data-driven approaches for reducing computational costs, as drawing definitive conclusions from a two-degree-of-freedom system may be premature. Furthermore, the development of more suitable mathematical models tailored to experimental test cases would enhance the framework's experimental validation and practical utility.

7 ACKNOWLEDGEMENTS

M. McGurk acknowledges the support of EPSRC Doctoral Training Partnership studentship (No. 2581922). J. Yuan acknowledges the funding support of the Royal Academy of Engineering/Leverhulme Trust Research Fellowship (LTRF2223-19-150) and Royal Society Research Grant (RGS-R2-242419). The authors acknowledge the experimental data provided by Dr Kyoung Hyun

and and co-workers at the University of Bristol, which is available at `https://github.com/Kyounghyunlee/`

References

1. Abdelkefi, A., Vasconcellos, R., Marques, F., Hajj, M.: Modeling and identification of freeplay nonlinearity. Journal of Sound and Vibration (2012), volume 331, Issue 8,Pages 1898-1907,ISSN 0022-460X
2. Abdelkefi, A., Vasconcellos, R., Nayfeh, A.H., Hajj, M.R.: An analytical and experimental investigation into limit-cycle oscillations of an aeroelastic system. Nonlinear Dynamics **71**(1), 159–173 (2013). https://doi.org/10.1007/s11071-012-0648-z
3. Ahsan, Z., Dankowicz, H., Li, M., Sieber, J.: Methods of continuation and their implementation in the coco software platform with application to delay differential equations. Nonlinear Dynamics **107**(4), 3181–3243 (2022)
4. Aruliah, D.A., van Veen, L., Dubitski, A.: A parallel adaptive method for pseudo-arclength continuation. In: Journal of Physics: Conference Series. vol. 385, p. 012008. IOP Publishing (2012). https://doi.org/10.1088/1742-6596/385/1/012008
5. Bauchau, O.A., Rodriguez, J., Bottasso, C.L.: Modeling of unilateral contact conditions with application to aerospace systems involving backlash, freeplay and friction. Mechanics Research Communications **28**(5), 571–599 (2001)
6. Bayer, F., Leine, R.I.: Sorting-free hill-based stability analysis of periodic solutions through koopman analysis. Nonlinear Dynamics **111**(9), 8439–8466 (2023). https://doi.org/10.1007/s11071-023-08247-7
7. Beregi, S., Barton, D.A., Rezgui, D., Neild, S.A.: Robustness of nonlinear parameter identification in the presence of process noise using control-based continuation. Nonlinear Dynamics **104**(2), 885–900 (2021). https://doi.org/10.1007/s11071-021-06347-w
8. Blyth, M., Renson, L., Marucci, L.: Tutorial of numerical continuation and bifurcation theory for systems and synthetic biology. arXiv preprint arXiv:2008.05226 (2020). https://doi.org/10.48550/arXiv.2008.05226
9. Cameron, T., Griffin, J.: An Alternating Frequency/Time Domain Method for Calculating the Steady-State Response of Nonlinear Dynamic Systems. Journal of Applied Mechanics (1989), american Society of Mechanical Engineers, ff10.1115/1.3176036ff. ffhal-01333697
10. Carslaw: Introduction to the theory of Fourier's series and integrals (Third ed.). New York: Dover Publications Inc. (1930)
11. Dahlke, J.A., Bettinger, R.A.: Practical implementation of pseudo-arclength continuation to ensure consistent path direction. Acta Astronautica **215**, 205–216 (2024). https://doi.org/10.1016/j.actaastro.2023.12.007
12. Dankowicz, H., Schilder, F.: Recipes for continuation. SIAM (2013). https://doi.org/10.1137/1.9781611972573
13. Detroux, T., Renson, L., Masset, L., Kerschen, G.: The harmonic balance method for bifurcation analysis of large-scale nonlinear mechanical systems. Computer Methods in Applied Mechanics and Engineering **296**, 18–38 (2015)
14. Dhooge, A., Govaerts, W., Kuznetsov, Y.A.: Matcont: a matlab package for numerical bifurcation analysis of odes. ACM Transactions on Mathematical Software (TOMS) **29**(2), 141–164 (2003)
15. Dhooge, A., Govaerts, W., Kuznetsov, Y.A., Meijer, H.G.E., Sautois, B.: New features of the software matcont for bifurcation analysis of dynamical systems. Mathematical and Computer Modelling of Dynamical Systems **14**(2), 147–175 (2008). https://doi.org/10.1080/13873950701742754
16. Dimitriadis, G.: Introduction to Nonlinear Aeroelasticity. Chichester: John Wiley & Sons Ltd. (2017). https://doi.org/10.1002/9781118756478
17. Doedel, E.J., Oldeman, B.: Auto-07p: continuation and bifurcation software. Montreal, QC: Concordia University Canada (1998), `https://github.com/auto-07p/auto-07p`
18. Edenborough, H.K.: Investigation of tilt-rotor vtol aircraft rotorpylon stability. Journal of Aircraft **5**(2), 97–105 (1968). https://doi.org/10.2514/3.43915

19. Edwards, J.W., Ashley, H., Breakwell, J.V.: Unsteady aerodynamic modeling for arbitrary motions. AIAA journal **17**(4), 365–374 (1979)
20. Gilioli, A., Manes, A., Ringertz, U., Giglio, M.: Investigation about the structural nonlinearities of an aircraft pylon. Journal of Aircraft **56**(1), 273–283 (2019). https://doi.org/10.2514/1.C034882
21. Govaerts, W.: Numerical bifurcation analysis for odes. Journal of computational and applied mathematics **125**(1-2), 57–68 (2000). https://doi.org/10.1016/S0377-0427(00)00458-1
22. Guckenheimer, J., Holmes, P.: Nonlinear oscillations, dynamical systems, and bifurcations of vector fields. Springer (2013). https://doi.org/10.1007/978-1-4612-1140-2
23. Gudmundson, P.: On the accuracy of the harmonic-balance method concerning vibrations of beams with nonlinear supports. Archive of applied mechanics (1991) **59**(5), 333–344 (1989). https://doi.org/10.1007/BF00534063
24. Guillot, L., Lazarus, A., Thomas, O., Vergez, C., Cochelin, B.: A purely frequency based floquet-hill formulation for the efficient stability computation of periodic solutions of ordinary differential systems. Journal of Computational Physics **416**, 109477 (2020). https://doi.org/10.1016/j.jcp.2020.109477
25. Hewitt, E., Hewitt, R.: The Gibbs-Wilbraham Phenomenon: An Episode in Fourier Analysis. Springer-Verlag (1979), archive for History of Exact Sciences, Volume 21
26. Howcroft, C., Lowenberg, M., Neild, S., Krauskopf, B., Coetzee, E.: Shimmy of an aircraft main landing gear with geometric coupling and mechanical freeplay. Journal of Computational and Nonlinear Dynamics **10**(5), 051011 (2015). https://doi.org/10.1115/1.4028852
27. Karkar, S., Cochelin, B., Vergez, C.: A comparative study of the harmonic balance method and the orthogonal collocation method on stiff nonlinear systems. Journal of Sound and Vibration **333**(12), 2554–2567 (2014). https://doi.org/10.1016/j.jsv.2014.01.019
28. Krack, M., Groß, J.: NLvib. University of Stuttgart (2020), available at: NLvib — Institut für Luftfahrtantriebe — Universität Stuttgart (uni-stuttgart.de) (Accessed 10/12/2021)
29. Krack, M., Salles, L., Thouverez, F.: Vibration prediction of bladed disks coupled by friction joints. Archives of Computational Methods in Engineering **24**, 589–636 (2017)
30. Lanza, V., Bonnin, M., Gilli, M.: On the application of the describing function technique to the bifurcation analysis of nonlinear systems. Circuits and Systems II: Express Briefs (2007), iEEE Transactions on, vol. 54, no. 4, pp. 343–347
31. Lazarus, A., Touzé, C.: A Harmonic-Based Method for Computing the Stability of Periodic Oscillations of Non-Linear Structural Systems. Proceedings of the ASME Design Engineering Technical Conference (2010), 5. 10.1115/DETC2010-28407.
32. Lazarus, A., Thomas, O.: A harmonic-based method for computing the stability of periodic solutions of dynamical systems. Comptes Rendus Mécanique **338**(9), 510–517 (2010). https://doi.org/10.1016/j.crme.2010.07.020
33. Lee, K., Barton, D., Renson, L.: Mathematical model identification of self-excited systems using experimental bifurcation analysis data. In: Nonlinear Structures & Systems, Volume 1: Proceedings of the 40th IMAC, A Conference and Exposition on Structural Dynamics 2022. pp. 61–63. Springer (2022)
34. Lee, K., Barton, D., Renson, L.: Modelling of physical systems with a hopf bifurcation using mechanistic models and machine learning. Mechanical Systems and Signal Processing **191**, 110173 (2023). https://doi.org/10.1016/j.ymssp.2023.110173
35. Li, H., Touzé, C., Gautier, F., Pelat, A.: Linear and nonlinear dynamics of a plate with acoustic black hole, geometric and contact nonlinearity for vibration mitigation. Journal of Sound and Vibration **508**, 116206 (2021). https://doi.org/10.1016/j.jsv.2021.116206
36. Liu, L., Dowell, E.: Harmonic Balance Approach for an Airfoil with a Freeplay Control Surface. Aiaa Journal - AIAA J. 43 (2005), 802-815. 10.2514/1.10973.
37. Mair, C.R.: Stability analysis of whirl flutter in rotor-nacelle systems with structural nonlinearities. Ph.D. thesis, University of Bristol (2021)
38. Masarati, P., Piatak, D.J., Quaranta, G., Singleton, J.D., Shen, J.: Soft-inplane tiltrotor aeromechanics investigation using two comprehensive multibody solvers. Journal of the American Helicopter Society **53**(2), 179–192 (2008). https://doi.org/10.4050/JAHS.53.179

39. Mauroy, A., Mezić, I.: Global stability analysis using the eigenfunctions of the koopman operator. IEEE Transactions on Automatic Control **61**(11), 3356–3369 (2016)
40. McGurk, M., Lye, A., Renson, L., Yuan, J.: Data-driven bayesian inference for stochastic model identification of nonlinear aeroelastic systems. AIAA Journal pp. 1–17 (2024). https://doi.org/10.2514/1.J063611
41. McGurk, M., Yuan, J.: Computation of limit cycle oscillations and their stabilities in nonlinear aeroelastic systems using harmonic balance methods. In: International Forum on Aeroelasticity and Structural Dynamics (IFASD) 2022 (2022)
42. Mezić, I.: Koopman operator, geometry, and learning of dynamical systems. Not. Am. Math. Soc. **68**(7), 1087–1105 (2021)
43. Mezić, I., Banaszuk, A.: Comparison of systems with complex behavior. Physica D: Nonlinear Phenomena **197**(1-2), 101–133 (2004)
44. Padmanabhan, M.A.: Sliding wear and freeplay growth due to control surface limit cycle oscillations. Journal of Aircraft **56**(5), 1973–1979 (2019)
45. Padmanabhan, M.A., Dowell, E.H., Pasiliao, C.L.: Computational study of aeroelastic limit cycles due to localized structural nonlinearities. Journal of Aircraft **55**(4), 1531–1541 (2018). https://doi.org/10.2514/1.C034645
46. Patil, M.J., Hodges, D.H.: On the importance of aerodynamic and structural geometrical nonlinearities in aeroelastic behavior of high-aspect-ratio wings. Journal of Fluids and Structures **19**(7), 905–915 (2004). https://doi.org/10.1016/j.jfluidstructs.2004.04.012
47. Peletan, L., Baguet, S., Torkhani, M., Jacquet-Richardet, G.: A comparison of stability computational methods for periodic solution of nonlinear problems with application to rotordynamics. Nonlinear Dynamics (2013), 72. 671-682. 10.1007/s11071-012-0744-0.
48. Peletan, L., Baguet, S., Torkhani, M., Jacquet-Richardet, G.: A comparison of stability computational methods for periodic solution of nonlinear problems with application to rotordynamics. Nonlinear dynamics **72**, 671–682 (2013)
49. Perroni, A.P., Bussamra, F.L.: Effects of geometric nonlinearity on flexible wing structures. Journal of Aircraft **58**(1), 85–97 (2021). https://doi.org/10.2514/1.C035745
50. Phillips, W., Alley, N., Niewoehner, R.: Effects of nonlinearities on subsonic aerodynamic center. Journal of aircraft **45**(4), 1244–1255 (2008). https://doi.org/10.2514/1.34241
51. Prokop, B., Frolov, N., Gelens, L.: Data-driven reconstruction of limit cycle position provides side information for improved model identification with sindy. arXiv preprint arXiv:2402.03168 (2024). https://doi.org/10.48550/arXiv.2402.03168
52. Razzak, M.A.: A simple harmonic balance method for solving strongly nonlinear oscillators. Journal of the Association of Arab Universities for Basic and Applied Sciences **21**, 68–76 (2016). https://doi.org/10.1016/j.jaubas.2015.10.002
53. Schinas, P., Manolas, D., Riziotis, V., Voutsinas, S.: Aeroelastic modal dynamics of floating wind turbines in anisotropic conditions based on floquet analysis. In: Journal of Physics: Conference Series. vol. 2265, p. 042005. IOP Publishing (2022). https://doi.org/10.1088/1742-6596/2265/4/042005
54. Seydel, R.: Practical bifurcation and stability analysis, vol. 5. Springer Science & Business Media (2009). https://doi.org/10.1007/978-1-4419-1740-9
55. Shearer, P.: Deep earth structure-seismic scattering in the deep earth. Seismology and the Structure of the Earth **1**, 695–729 (2007)
56. Tartaruga, I., Cooper, J., Lowenberg, M., Sartor, P., Lemmens, Y.: Uncertainty and sensitivity analysis of bifurcation loci characterizing nonlinear landing-gear dynamics. Journal of Aircraft **55**(1), 162–172 (2018). https://doi.org/10.2514/1.C034252
57. Tartaruga, I., Barton, D.A., Rezgui, D., Neild, S.A.: Experimental bifurcation analysis of a wing profile. In: International Forum on Aeroelasticity and Structural Dynamics: IFASD 2019 (2019), `http://ifasd2019.utcdayton.com/`
58. Teschl, G.: Ordinary differential equations and dynamical systems, vol. 140. American Mathematical Soc. (2012). https://doi.org/10.2991/978-94-6239-021-8
59. Theodorsen, T.: General Theory of Aerodynamic Instability and the Mechanism of Flutter. NACA Rept (1935), 496.
60. Trickey, S.T., Virgin, L., Dowell, E.: The stability of limit–cycle oscillations in a nonlinear aeroelastic system. Proceedings of the Royal Society of London. Series A: Mathematical, Physical and Engineering Sciences **458**(2025), 2203–2226 (2002). https://doi.org/10.1098/rspa.2002.0965

61. Wright, J., Cooper, J.: Introduction to Aircraft Aeroelasticity and Loads. 2nd edn. Chichester: John Wiley & Sons Ltd (2014). https://doi.org/10.1002/9781118700440, chapter 10.4

A Model parameters

Table 2: Parameters used in case study

	Numerical		Experimental	
Parameter	Smooth	Nonsmooth	Configuration 1	Configuration 2
$b\ (m)$	0.127	0.127	0.150	0.150
a	-0.5	-0.5	-0.5	-0.5
$m_w\ (kg)$	1.56	1.56	5.30	5.30
x_α	0.434	0.434	0.24	0.24
$I_\alpha\ (kg.m^2)$	0.001347	0.001347	0.1724	0.1724
$K_h\ (N/m)$	2818.8	2818.8	3529.4	3318.3
$K_\alpha\ (N/rad)$	0	0	54.11	65.6
$c_h\ (kg/s)$	0.77	0.77	14.58	14.58
$c_\alpha\ (kg.m^2/s^2)$	0.63	0.63	0.56	1.03
$c_w\ (kg/s)$	0.54	0.54	0	0
c_1	0.165	0.165	0.165	0.165
c_2	0.0455	0.0455	0.0455	0.0455
c_3	0.335	0.335	0.335	0.335
c_4	0.3	0.3	0.3	0.3
$K_{\alpha 2}\ (N/rad^2)$	250	-	751.6/524.50	774.7/678.32
$K_{\alpha 3}\ (N/rad^3)$	7500	-	5006.7/2595.9	3490.7/ 2982.6
$\delta\ [rad]$	-	0.0175	-	-
$V_f\ (m/s)$	31.45	31.45/29.50	17.80	26.15